Unveiling the Evolution of Extreme Rainfall Across Space and Time in a Warming Climate

Ankit Ghanghas[1], Ashish Sharma[2], and Venkatesh Merwade[1]

[1] Lyles School of Civil Engineering, Purdue University, West Lafayette, IN, USA

[2] School of Civil and Environmental Engineering, University of New South Wales, Sydney, New South Wales, Australia.

Corresponding author: Ankit Ghanghas (aghangha@purdue.edu)

Key Points:

- Introduces Spatio-Temporal Homogeneity metric to effectively track comprehensive changes in storm characteristics across both space and time.
- Rising temperature results in "smaller and peakier" storms in the tropics, intense precipitation burst in smaller area over shorter duration.
- Rising temperatures leads to front-loaded storms, notably in tropics and southern temperate regions, potentially increasing flash flood risk

Abstract.

Climate change induces significant changes in storm characteristics, particularly for short-duration extreme storms, impacting their intensity and spatio-temporal distribution. Although alterations in precipitation intensity are well documented, past studies examining changes in spatio-temporal distribution of storms were region-specific and focused on isolated aspects of change in space or time, eluding a comprehensive understanding of the precise nature and extent of these changes. Bridging this gap, this study introduces a novel grid-based measure of storm homogeneity, the spatio-temporal homogeneity and investigates the global patterns of change in combined spatio-temporal characteristics of short duration extreme storms. Analyzing the 30min X 0.1° X 0.1° resolution Global Precipitation Measurements, the study finds that extreme storms are shrinking in both space and time due to rising surface air temperatures, predominantly in tropics. In contrast, temperate regions experience expanded extreme storms with increasing temperatures. The study also identifies a global prevalence of front-loaded storms with rising temperatures, driven by a substantial increase in tropics and southern temperate regions. Conversely, storms in northern temperate regions become uniform or slightly rear-loaded as temperature increases. Furthermore, the study finds that characteristics of short–duration storms (6–12 hours) are more sensitive to temperature changes. Overall, this study contributes valuable insights into the global spatio-temporal changes of short duration extreme storms, highlighting regions most susceptible to alterations in storm patterns due to climate change. These findings are essential for developing effective adaptation strategies and flood management practices to cope with the changing nature of extreme storms in a warming climate.

1 Introduction.

Changes in intensity and frequency of rainfall have significant implications for ecosystem services, water resources availability and agricultural production. Accumulating evidence points towards an increase in intensity and frequency of extreme precipitation events within a warming climate along with a change in its distribution in time and space (Fischer & Knutti, 2016; Guerreiro et al., 2018; Masson-Delmotte et al., 2021; Wang et al., 2017; Wasko et al., 2023; Westra et al., 2014). This trend raises legitimate concerns as floods may become potentially more frequent and severe (Sharma et al., 2018; Wasko & Nathan, 2019). In a warming climate, the intensity of extreme precipitation will increase in line with the rise in atmospheric moisture, as governed by the Clausius-Clapeyron relation (CC rate). However, some regions, particularly tropics and subtropics have experienced even greater increases in precipitation intensity than what can be accounted for by the CC rate (Berg et al., 2009; Emori & Brown, 2005; Fowler et al., 2021; J. B. Visser et al., 2021). This phenomenon, known as super CC scaling (>CC rate), is particularly prominent for sub-hourly or sub-daily short duration precipitation extremes (Berg et al., 2013; Fowler et al., 2021; Lenderink & van Meijgaard, 2008; Mishra et al., 2012). The super CC scaling is hypothesized to be a result of change in storm dynamics as dictated by the changes in spatial and temporal signatures of storms (Collins et al., 2013; Fowler et al., 2021; Lenderink & van Meijgaard, 2008).

To understand the changes in precipitation under rising temperatures, numerous recent studies have investigated the intensification of spatial and temporal patterns of precipitation. Wasko and Sharma (2015) investigated the correlation between temperature and the temporal patterns of precipitation with varying durations across Australia. Their findings revealed that higher temperatures are associated with less uniform temporal patterns of precipitation, characterized by more intense peak precipitation and weaker precipitation during less intense periods (Figure 1a). This phenomenon of a "peakier" temporal pattern was particularly pronounced in tropical regions and was amplified with increased durations of storm. This peakier temporal pattern was also linked to a decrease in the storm volume, possibly because the storms analyzed became shorter in duration as temperature increased. Another study (Long et al., 2021) analyzed complete precipitation events across humid region of China using a temporal concentration index (TCI), and found similar patterns of temporal concentration of precipitation as temperatures increased within a range of 5-24°C before plateauing at higher temperatures.

Some other studies focused on analyzing changes to the spatial patterns of precipitation (Figure 1b). The effect of temperature on the spatial extent of extreme storms can vary depending on the study region, type of storm and duration of precipitation extreme. While some studies show an increase in spatial extent with rising temperature (Bevacqua et al., 2021; Chen et al., 2021; Lochbihler et al., 2017; Matte et al., 2022), numerous others found a decrease in spatial extent (Chang et al., 2016; Li et al., 2018; Peleg et al., 2018; Wasko et al., 2016). A recent study by Ghanghas et al. (2023) found an overall global trend of decrease in spatial extent with increasing temperature for sub-hourly extreme storms. They also found that spatial extent of storms in Arid regions and parts of central Europe increased with increasing temperature. Similar trends of decreasing spatial extent with temperature were observed for humid regions in China using spatial concentration index (SCI)(Long et al., 2021)

It is worth noting that the studies investigating changes in spatial and temporal patterns of precipitation have typically focused purely on either spatial changes or temporal changes, without providing a comprehensive analysis of changes in both space and time. Even Long et al. (2021), in their attempt to analyze the spatio-temporal structure of precipitation events, employed two separate metrics to assess changes in spatial structure and temporal structure independently. This fragmented approach limits our understanding of the holistic changes occurring in precipitation patterns in response to rising temperatures. Furthermore, while these studies suggest a spatial and temporal intensification of the events, they fail to preserve the natural spatio-temporal structure of the event itself and provide no information on lateral shift (or "event loading") in precipitation. The timing of occurrence of bulk precipitation or "event loading", is one of the defining characteristics of spatio-temporal distribution of the precipitation storm and can play a key role in design flood estimation (Fadhel et al., 2018; Hettiarachchi et al., 2018; J. Visser et al., 2023). Visser et al. (2023) used a novel D_{50} approach to analyze the changes in event loading of temporal patterns for extreme storms in Australia. They found that rising temperatures leads to a distinct shift towards increased front-loaded temporal patterns of precipitation, particularly in tropical regions. However, this study was limited to storms in Australia and focused on event loading with respect to only temporal patterns of precipitation. The effect of climate change on "event loading" in terms of changes in both space and time has not been explored in past studies.

104 While mounting evidence supports the increase in intensity and frequency of extreme
105 storms in a warming climate, there is a lack of holistic understanding of changes in spatio-
106 temporal patterns of these storms. Such insights about the spatio-temporal pattern of storms are
107 pivotal for accurate flood behavior simulation (Gao & Fang, 2019; Ogden & Julien, 1993; Shah
108 et al., 1996; V. P. Singh, 1997). Consequently, this deficiency in understanding the nuanced
109 spatio-temporal shifts within storms has resulted in very little knowledge on how hydrological
110 applications should accommodate the changes induced from a warming climate. In an effort to
111 bridge this gap and gain a more comprehensive understanding of the changes occurring in
112 precipitation patterns, this study investigates the combined changes in spatio-temporal patterns of
113 extreme precipitation events across the globe. Specifically, the study attempts to answer the
114 following questions. (i) How can one effectively summarise change in spatio-temporal extent for
115 an extreme storm, while ensuring this summary is scale independent and comparable across time
116 and space? ii) How does the spatio-temporal extent of extreme storms change with rising
117 temperatures? Do storms get more localized and peakier, or do they exhibit more uniformity and
118 spread in space and time (Figure 1c). iii) Which climatic regions observe peakier and localized
119 storms as the temperatures rise? iv) How does rising temperature effect the spatio-temporal
120 distribution ("event loading") of extreme storms and whether storms get more front-loaded or
121 rear-loaded in terms of their spatio-temporal distribution (Figure 1d)? v) Is the effect of
122 temperature on spatio-temporal patterns independent of storm duration? Which durations storms
123 exhibit highest levels of asymmetry and localization? These objectives are achieved by
124 introducing a novel metric termed Spatio-Temporal Homogeneity (STH) on the 30-min
125 Integrated Multi-satellite Retrievals for Global Precipitation Measurement (IMERG) dataset. The
126 metric is based on the Spatial Homogeneity (SH) metric used by Ghanghas et al. (2023) and
127 follows an enhanced rationale to extend into the temporal dimension. STH quantifies the grid
128 homogeneity around the extreme storm in both space and time, and can be used to compare
129 changes in spatio-temporal distribution of extreme storms with different intensities and at
130 different locations.
131

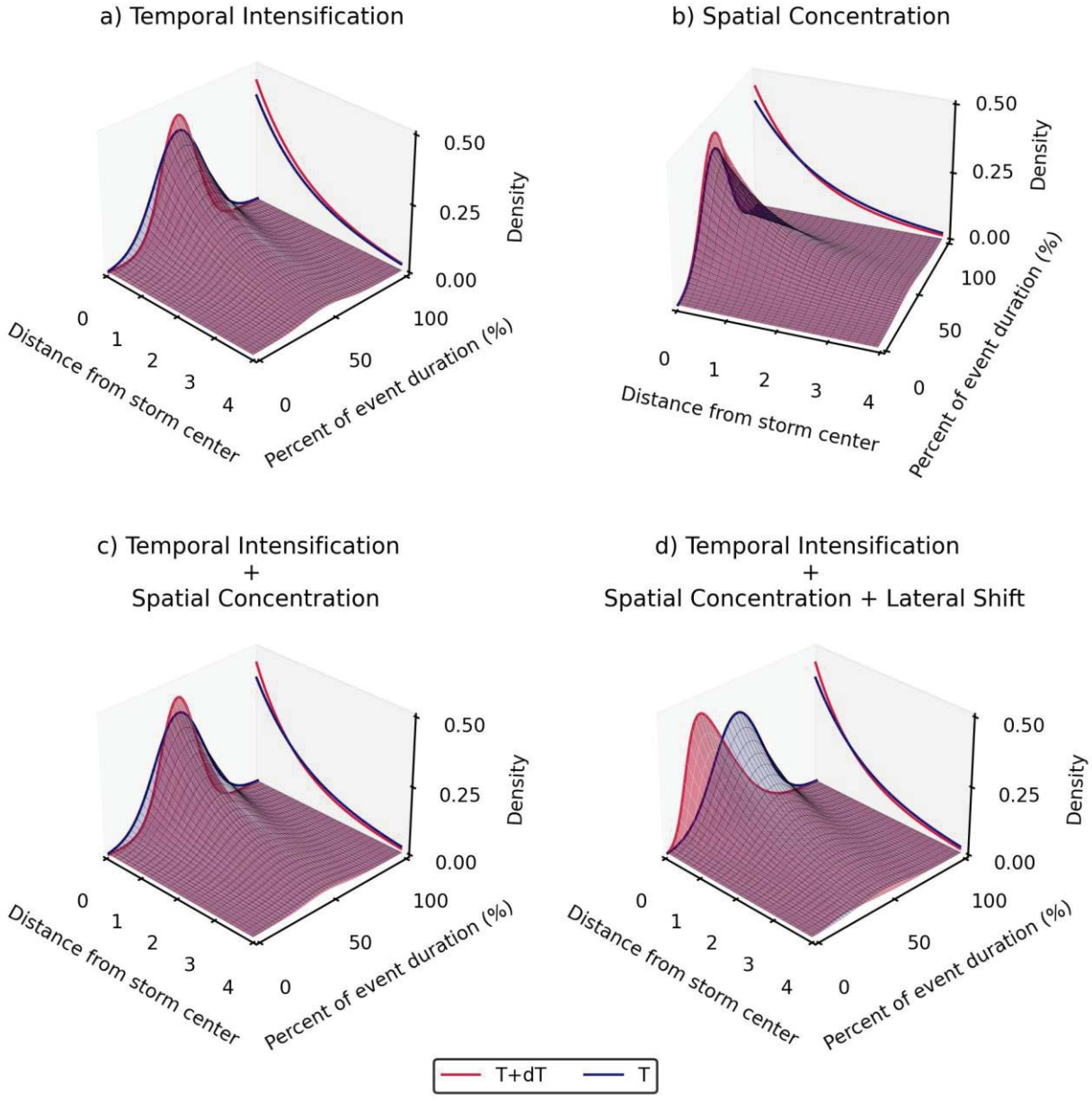

Figure 1 *Precipitation distribution of an extreme storm in space and time (3D surfaces) and individual distribution in space or time (lines) on the 2D projected planes, for conceptual precipitation events of equal duration. Blue surface and lines represent base storm occurring at a cooler temperature, Red surface and lines represent intensified storm occurring at a warmer temperature. a) Traditional temporal intensification with spatial distribution of precipitation increasing proportionately to increase in peak precipitation. b) Spatial Concentration of precipitation towards the spatial center of the storm, no temporal intensification/concentration. c) Temporal intensification along with spatial concentration of the storm, storm concentrating in both space and time. d) Temporal and spatial concentration of the storm along with a lateral shift in spatio-temporal distribution of precipitation.*

2 Data and Methods

2.1 Meteorological data

To ensure a comprehensive global analysis of changes in spatio-temporal distribution of extreme precipitation events, the study utilizes satellite precipitation data from the IMERG dataset (or Global Precipitation Measurements, GPM), instead of sparsely gauged ground observations. The use of GPM is motivated by its high spatio-temporal resolution, global coverage and continuous records from 2000 to present, thus enabling the global assessment of changes in spatio-temporal patterns. Although it should be noted that GPM tends to underestimate and under detect low precipitation events, particularly in mountainous and arid regions; it exhibits improved performance for higher intensity and spatially widespread events in these regions (Bulovic et al., 2020; Libertino et al., 2016). Additionally, IMERG has been found to provide a reliable representation of spatial coverage and precipitation intensities (Beck et al., 2019; Lau & Behrangi, 2022; Sungmin et al., 2017; Tan et al., 2018; Wati et al., 2022), surpassing other satellite and reanalysis products, especially for estimates of hourly and sub-hourly precipitation (Tang et al., 2020).

This study uses IMERG's high spatial and temporal resolution 3IMERGHH (version 6) product available at 0.1° X 0.1° spatial resolution and 30-minute time interval (Huffman et al., 2020), from 2005 to 2021. Additionally, hourly 2m surface air temperature available at 0.1° X 0.1° spatial resolution from Earth ReAnalysis Land (ERA5-Land, (Muñoz-Sabater et al., 2021) is used. ERA5-Land is the land component of the global reanalysis ERA5 data produced by the European Center for Medium-Range Weather Forecasts (ECMWF). ERA5 combines historical observations with the Integrated Forecasting System (IFS) Cy41r2 model to produce hourly outputs of numerous atmospheric, land and oceanic climate variables (Hersbach et al., 2020).

2.2 Extreme storm selection

In order to examine the spatio-temporal structure of extreme precipitation events, events independent in both space and time must be identified. The process of achieving independence in both space and time is conducted in three steps. First, temporally independent events are identified for each grid cell in the GPM dataset. Temporal independence of these events at each grid cell is ensured by selecting events that are separated by a minimum period of zero rainfall or minimum inter-event time (IE time). The choice of IE time is crucial, as smaller values limit intra-event intermittency while larger values ensure event independence. In this study, IE time of

1hr and 5hr are employed to assess the impact of choosing different IE times on changes in spatio-temporal structure under warming environments. The IE time also helps determine the start and end of the event, which is used to estimate the event duration (or storm duration).

Next, from the set of temporally independent events obtained in the previous step, the ten highest 30-min Annual Maxima Precipitation (30-min AMP) events are selected for each cell in the GPM dataset. For each of these events, a storm field is defined in the form of a 9-cell grid by including the cell with the extreme precipitation event and its eight neighboring cells. The independence of the storm field and consequently the independence of events in space is enforced by selecting events in which the center pixel of the storm field receives greater precipitation than the surrounding cells (Ghanghas et al., 2023). The events selected after completing the first and second steps exhibit discrete independence in space and time.

Finally, to ensure joint independence in space and time, a condition is imposed. Specifically, the time of peak of the storm centered in any storm field must not coincide over the storm duration (the period between start and end of storm event) of a storm centered at any neighboring cell. For any cell in the GPM data, only one extreme storm with the highest 30-min precipitation intensity among all events satisfying all these conditions per year is finally chosen for analysis.

2.3 *Spatio-Temporal Homogeneity*

Building on the two-dimensional spatial homogeneity (SH) metric (Ghanghas et al., 2023), this study develops a three-dimensional Spatio-Temporal Homogeneity (STH) metric. STH allows investigation and comparison of changes in spatio-temporal signatures of extreme storms with varying intensity and at different locations. To evaluate the spatio-temporal characteristics of the extreme storm at any grid cell, precipitation is sampled in the storm field (9 cell grid) at seven different time intervals. Assuming, 't_0' represents the time of arrival of the storm peak at center grid cell, precipitation is sampled at three-time intervals before 't_0' (9 hours(t_{-9}), 6hours(t_{-6}) and 3 hours(t_{-3})), at the time of the peak itself, and at three-time intervals after 't_0' (3hours(t_{+3}), 6hours(t_{+6}) and 9 hours(t_{+9})). Since at each time interval, precipitation is sampled across the entire storm field (9 cell grid), this results in 63 (9 cells x 7 time intervals) precipitation samples for each storm. This forms a three-dimensional kernel (3x3x7) with two space dimensions representing the spatial variation and one time dimension representing the evolution of storm in time.

In order to capture the spatial distribution of the storm, each cell in the spatial field is assigned a suitable weight (W_s) based on its spatial proximity to the storm center. Weights are assigned based on inverse distance between the center of the cell to the storm center. This results in higher weightage to precipitation close to the storm center. Similarly, to represent the temporal signature, each timestep is assigned a suitable weight (W_t) to reflect their temporal proximity to the storm peak. For precipitation sampled at 't_{-9}' (or 't_{+9}'), a weight of 1/1.9 (0.526) is assigned; for precipitation sampled at 't_{-6}' (or 't_{+6}') the weight equals 1/1.6, and so on. Precipitation sampled at 't_0', time of peak of storm, gets a weight of 1. While other weights can also be used to preserve the spatial and temporal signature, it is found that using different weights does not result in statistically different responses in terms of sensitivity of spatio-temporal characteristics to temperature.

Precipitation in all cells of the three-dimensional spatio-temporal kernel (3x3x7) are ranked in ascending order and each cell is then multiplied with its corresponding aggregated weight W_{agg} ($W_{agg} = W_s \; x \; W_t$). Similar to the spatially accumulated precipitation average in the SH metric (Ghanghas et al., 2023), the spatio-temporally accumulated precipitation average (AcP) is determined by progressively expanding the kernel around the center of the storm peak. AcP is calculated using Equation 1.

$$AcP_{n,m} = \frac{\sum_{i=1}^{n}\sum_{t}^{m} P_{i,t} \; x \; W_{agg_{i,t}}}{\sum_{i=1}^{n}\sum_{t}^{m} W_{agg_{i,t}}} \quad (1)$$

where $P_{i,t}$ represents precipitation rank in i^{th} pixel in the storm field at t^{th} time interval, $t \in \{t_{-9}, t_{-6}, t_{-3}, t_0, t_{+3}, t_{+6}, t_{+9}\}$. i indicates the i^{th} highest precipitation rank in a storm field at a given time interval. n is the number of storm field cells used for spatio-temporal accumulation and m is the number of time intervals used for spatio-temporal accumulation.

$AcP_{9,7}$ represents the weighted average precipitation for the entire space-time kernel. The values of AcP are then plotted against the number of cells and number of time intervals considered in formulating AcP (Figure 2a). STH is formulated comparing the actual extreme storm to two possible extreme cases. The first reference case assumes precipitation occurs only at the center of the storm field and only at time t_0 (only $P_{0,t0}$ occurs and the rest are all zero). The first case presents the smallest possible spatio-temporal extent for the given peak intensity of the storm, i.e. an isolated storm with precipitation occurring only on a small region (one cell of GPM) and only at one recorded instant (30mins) (red surface in Figure 2a). The second reference

case assumes that all grid cells in the 3D kernel receive the same amount of precipitation as the center cell ($P_{0,t0}$ occurs at all time intervals and across all cells). The second reference case represents the largest possible spatio-temporal extent for the chosen kernel and the given peak intensity of the storm, i.e. a large uniform storm (Grey surface in Figure 2a). STH is then formulated by noting how strongly the actual extreme event deviated from first reference case (marked by 'a' in Figure 2a and Eq 2) with reference to the total possible deviation between the first and second refence case ('a+b' in Figure 2a and Equation 2). The Spatio-Temporal Homogeneity metric (STH) calculated using Equation 2 quantifies the degree of spatio-temporal homogeneity/inhomogeneity of the extreme storm. STH metric collapses to zero for more isolated and spatio-temporally intense storms while it tends to a value of one for more uniform extremes.

$$STH = \frac{a}{a+b} = \frac{\frac{\sum_{i=1}^{9}\sum_{t}^{7} P_{i,t}\ x\ W_{agg_{i,t}}}{\sum_{i=1}^{9}\sum_{t}^{7} W_{agg_{i,t}}} - \frac{P_{0,t_0}}{\sum_{i=1}^{9}\sum_{t}^{7} W_{agg_{i,t}}}}{P_{0,t_0} - \frac{P_{0,t_0}}{\sum_{i=1}^{9}\sum_{t}^{7} W_{agg_{i,t}}}} \quad (2)$$

2.4 *Event Loading*

Dominance of front or rear loading changes the spatio-temporal distribution of precipitation around the time of peak of the storm. When examining the temporal distribution of precipitation from reference of the peak of the storm, front loaded storms exhibit a sudden rise in precipitation leading up to the peak (steep rising limb similar to a hydrograph) which dissipates slowly after the peak (flatter falling limb signature) (Figure 2b). While on the other hand, rear loaded storms feature a flatter rising limb leading up to the peak, indicating slow rise in precipitation intensity, and then the precipitation dissipates suddenly after the peak (steep falling limb) (Figure 2c). The study exploits these differences in falling and rising limb to understand the event loading of the extreme storm.

According to the characteristics outlined by Visser et al. (2023) for a front-loaded storm, the rising limb of such a storm is spatio-temporally less uniform compared to the falling limb. So, if a hypothetical storm is constructed by mirroring rising limb of a front loaded storm about the peak, the spatio-temporal homogeneity (hence STH metric) of this mirrored storm would be less than the spatio-temporal homogeneity of the original storm (Figure 2b). The degree of event loading (EL) for the original storm can therefore be estimated as percentage deviation in STH for rising limb mirrored storm from original storm STH with reference to original storm STH (Eq 3).

$$Event\ Loading\ (EL)(\%) = \frac{STH_{rising\ limb\ mirrored} - STH_{original}}{STH_{original}} \times 100 \quad (3)$$

Similarly, STH for a hypothetical storm constructed by mirroring the rising limb of a rear-loaded storm would be larger than STH for the original storm. The EL metric proposed here effectively captures the timing of bulk precipitation. A positive EL indicates a rear-loaded event whereas a negative EL indicates a front-loaded event.

2.5 *Relating Spatio-Temporal Characteristics to Temperature.*

The variability of spatio-temporal characteristics, including event loading and STH, of extreme storms are analyzed by pairing the extreme storm events with the representative storm temperature. The representative storm temperature is computed by taking the mean surface air temperature averaged over the 12-hour period leading up to the start of the extreme storm. Henceforth, this representative mean surface air temperature is referred to as "temperature". This approach aligns with the recommendations proposed by (J. B. Visser et al., 2020) which suggests that taking mean of temperatures leading up to the storm minimizes the cooling effects of the precipitation event itself, and is also representative of the variability in precipitation intensities.

The sensitivity of storm characteristics (STH and event loading) with temperature is performed using quantile regression (Koenker & Bassett, 1978). Quantile regression is preferred over traditional binning techniques and least square methods due to its ability to provide unbiased and robust estimates (Wasko & Sharma, 2014). This study focuses on the 50th percentile (median) instead of rarer percentiles since only one extreme event per year is considered. The sensitivity of storm characteristics with temperature (T) is calculated using Eq 4.

$$y = \beta_0^q + \beta_1^q T \quad (4)$$

where y is the storm characteristic (STH /event loading), β_0 and β_1 are fitted parameters and q is the target quantile (0.5 for this study). The sensitivity of the characteristic with temperature is then quantified as 100x $\beta_1 q$, expressed in percentage. To ascertain the statistical significance of the observed trends, sensitivity of STH and EL to temperature is computed by ordering the metrics in ascending order of temperature and then evaluating the statistical significance using Mann-Kendall Test at 5% significance. This sensitivity is computed exclusively for cells presenting statistically significant trend in the metric (STH or EL), and the results are then presented after applying a 4° × 4° moving median on the sensitivity to smooth out the variability.

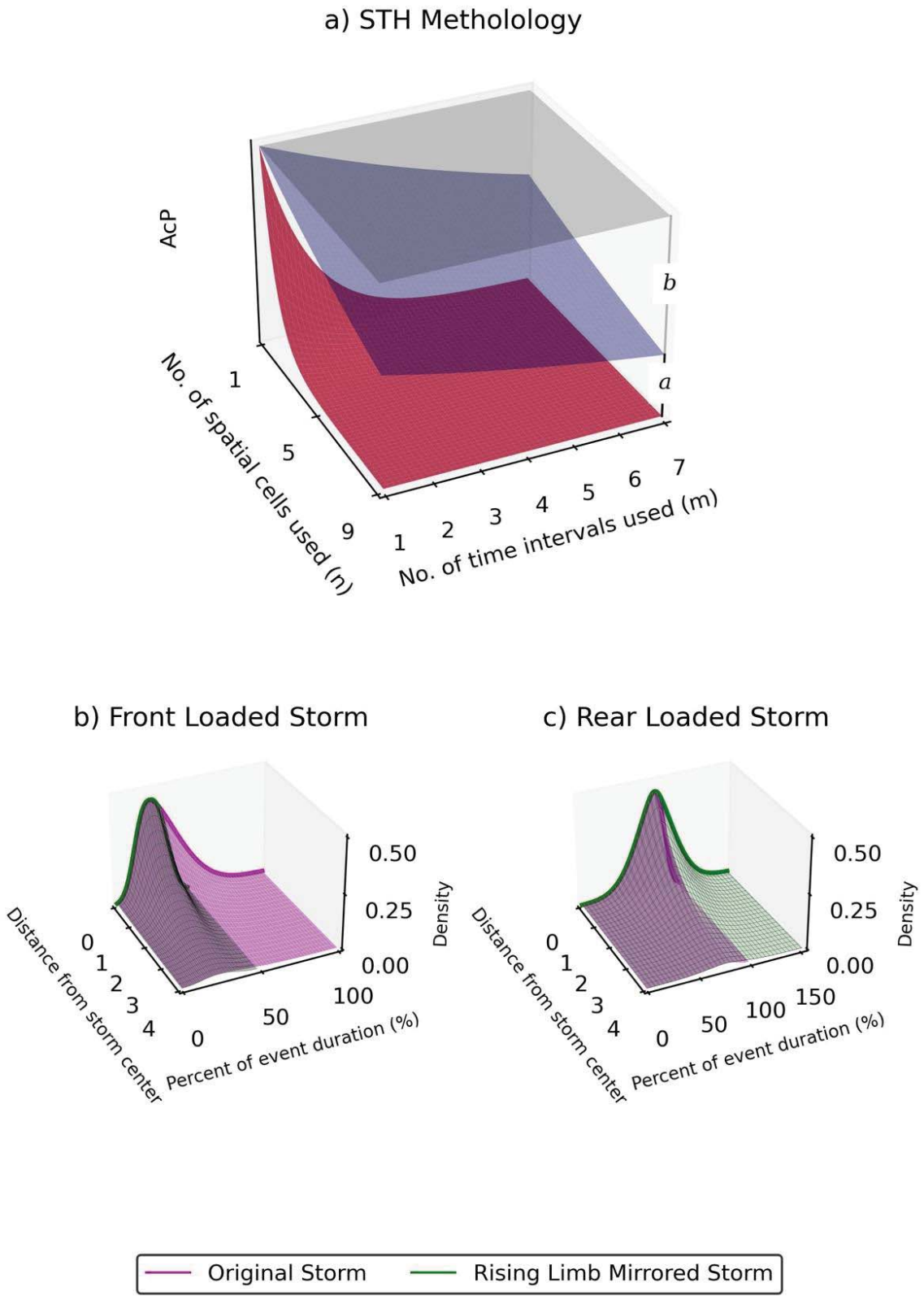
a) STH Methodology
AcP
b
a
No. of spatial cells used (n)
1
5
9
1
2
3
4
5
6
7
No. of time intervals used (m)
b) Front Loaded Storm
c) Rear Loaded Storm
Distance from storm center
0
1
2
3
4
Percent of event duration (%)
0
50
100
150
Density
0.50
0.25
0.00
Original Storm
Rising Limb Mirrored Storm

Figure 2 *a) Methodology of STH. As more cells in space and time are included, the red, blue and grey surface show the changes in accumulated weighted precipitation average (AcP) for storm precipitating only at one grid cell and just one time step, original storm to be analyzed, and storm precipitating with same intensity across all grid cells and all-time steps in the space time kernel respectively. b) and c) Methodology of event loading. Purple surface presents the precipitation distribution of original storm to be analyzed and green surface presents the precipitation distribution of rising limb mirrored storm.*

3 Results.

3.1 STH and temperature Relations.

The STH metric, while not providing a quantitative estimate of the precise spatio-temporal extent of storms, serves as a quick and resourceful method for monitoring alterations in this extent and gauging the sensitivity of these changes to shifts in climatic factors. An examination of the median STH metric for AMP 30-minute storms reveals occurrence of temporally shorter storms in mountainous and arid regions globally (Figure S1 in supplementary information). However, since the study primarily focuses on understanding how changes in climate influence the spatio-temporal distribution of storms, the analysis centers on comprehending the variation in spatio-temporal distribution in response to changing temperatures. Consequently, the study explores the sensitivity of STH to temperature while also endeavoring to discern regional patterns through the regionalization of results across the 33 IPCC AR5 regions (Figure 3).

The global median sensitivity of STH to temperature is estimated as - 0.16 % / °C, revealing an overall trend of slight decrease in STH with temperature. However, the overall trends provide very limited insight into the geographic variation in these sensitivities. To gain a better understanding of the geographic variation in the sensitivity of STH to temperature, Figure 4 presents global maps of STH sensitivity with temperature (Figure 4a). Additionally, Figure 4b presents boxplots of STH sensitivity with temperature for 32 out of the 33 IPCC AR5 regions (Figure 3). Due to small geographical extent of islands in NTP*, no sensitivity of STH could be estimated for the region.

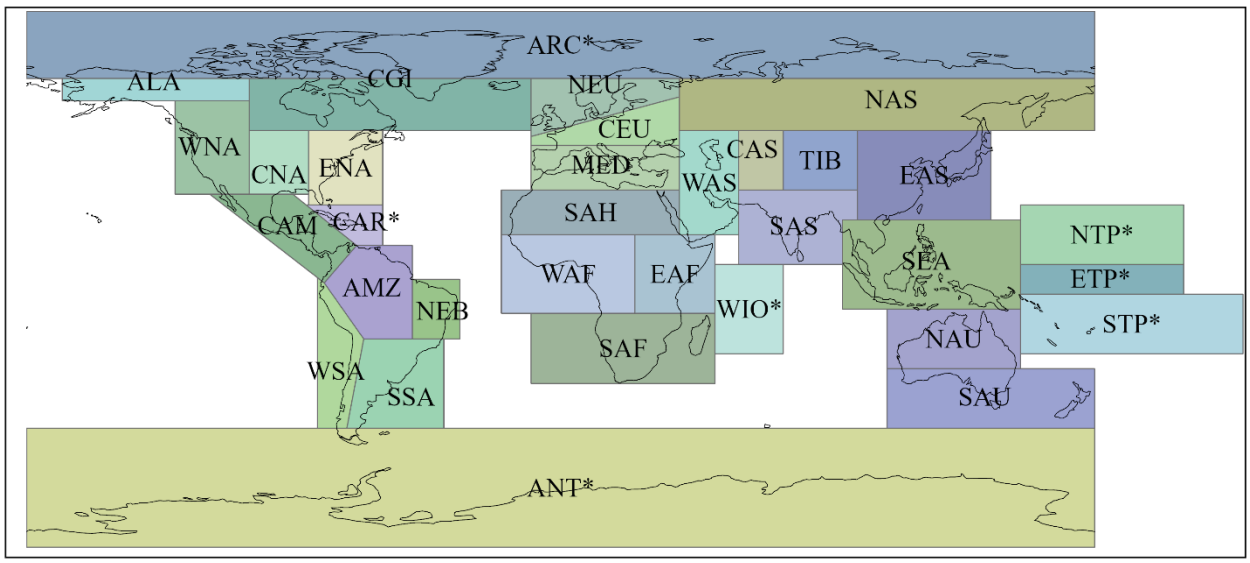

Figure 3. *Thirty three regions used by Intergovernmental Panel on Climate Change (IPCC)'s Fifth Assessment Report (AR5;*(Seneviratne et al., 2012)*). The 33 regions comprise of 26 Special Report on Climate Extremes (SREX) regions and 7 non-SREX regions (marked by *). Here, ALA: Alaska/N.W. Canada, AMZ: Amazon, CAM: Central America/Mexico, CAR*: Caribbean, CAS : Central Asia, CEU: Central Europe, CGI: Canada/Greenland/Iceland, CNA: Central North America, EAF: East Africa, EAS: East Asia, ENA: East North America, MED: South Europe/Mediterranean, NAS: North Asia, NAU: North Australia, NEB: North-East Brazil, NEU: North Europe, SAF: Southern Africa, SAH: Sahara, SAS: South Asia, SAU: South Australia/New Zealand, SEA: South East Asia, SSA: Southeastern South America, TIB: Tibetan Plateau, WAF: Western Africa, WAS: West Asia, WNA: West North America, WSA: West Coast South America, ANT*: Antarctica, ARC*: Arctic, NTP* Pacific Islands region, STP*: Southern Tropical Pacific, ETP*: Pacific Islands region, WIO*: West Indian Ocean.*

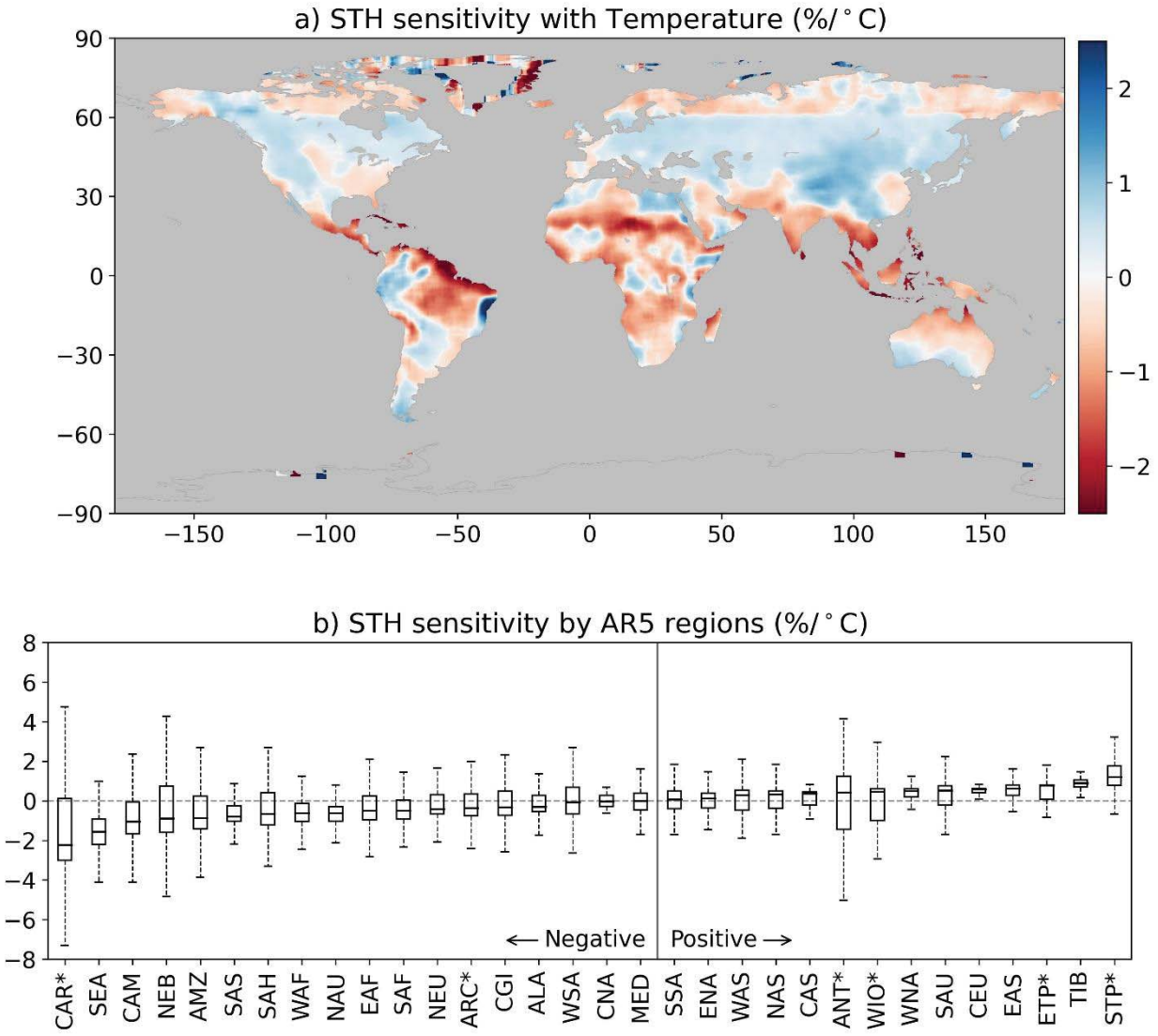

Figure 4 *Results of sensitivity of STH with temperature for 5hr IE time. A) 4x4° median STH sensitivity with temperature b) Variation in STH sensitivity with temperature for different IPCC AR5 regions.*

The trend of global median sensitivity is largely driven by notable negative STH sensitivity observed around the equator (between 30°N and 30°S) (Figure 4a). These tropical regions, where extreme precipitation is largely dominated by convective storms, observe a reduction in spatio-temporal extent of the storm as temperature increases. Significant negative sensitivity is observed in Amazon, western Africa around the Gulf of Guinea, Madagascar Island, Central America and the caribbean, India and Southeast Asian Archipelago. Notable negative STH sensitivity is also observed in parts of Sahara. The magnitude of negative STH decreases and turns to positive as the analysis moves further away from the tropics. It is essential to emphasize

that this negative STH sensitivity tends to occur primarily in regions with higher mean annual temperature, where the storms occur in warmer conditions compared to temperate regions. Additionally, these regions are associated either with high humidity (tropics) or with low humidity (arid Sahara). Away from the tropics, STH moderately decreases with temperature in the eastern United States, as the extreme precipitation in these regions are largely caused by tropical cyclones landing in the region in the summer season. Moderate negative STH sensitivity is also observed in parts of midwestern United States, close to the great lakes, as well as in western Europe (including England, France, Portugal, and Spain) and the northern Australia. Excluding the above-mentioned regions, the storms in the Northern and Southern temperate regions (beyond 30°N and 30°S) generally tend to expand in space and time (positive STH sensitivity) with increasing temperature. This positive sensitivity in the temperate regions is less prominent compared to the negative sensitivity in the tropics.

Segmenting the trend magnitudes by the 33 IPCC AR5 regions (Seneviratne et al., 2012), the results are presented as boxplots in Figure 4b. A total of 18 regions from CAR* to MED have negative median STH sensitivity and are presented on the left, while a total of 14 regions from SSA to STP* have positive median STH sensitivity and are presented on the right. Among them, except for the seven non-SREX regions marked by asterisks in the boxplot, the three regions showing the largest negative STH sensitivity are SEA (South East Asia), CAM (Central America), and NEB (North-East Brazil), while the three regions showing greatest positive sensitivity are TIB (Tibet), EAS (East Asia) and CEU (Central Europe). These AR5 regions help understand the overall regional variation, however they encompass large areas and can sometimes result in negligible overall median sensitivity. For instance, large parts of CNA (Central North America) and ENA (East North America) exhibit some negative STH sensitivity, but some other parts show positive sensitivity thus resulting in an overall negligible median sensitivity for the region. Particularly for CNA and ENA, negative sensitivity is observed in cyclone dominated areas, while positive sensitivity is observed in temperate parts of the region where extreme storms are more dependent on low pressure systems and atmospheric river. Similar behavior is also observed in WSA (West South America), MED (Mediterranean) and SSA (Southern South America).

The aforementioned results are based on an IE time of 5 hours. However, it is possible that the sensitivity of STH may change with different IE times, as choosing appropriate IE time

is key in balancing intra event intermittency and event independence. Thus, to assess the impact of choosing a small versus a large IE time, the study compared the STH sensitivity with temperature for two IE times, 1hr and 5hr (Figure 5). The selection of these IE times aligns with those used in previous studies (Visser et at., 2021; Wasko et al., 2015). The results clearly indicate that selecting different interevent time does not alter the behavior of changes in spatio-temporal characteristics of storms under warming environments. Areas showing negative/positive STH sensitivity consistently show negative/positive sensitivity regardless of the IE time used to separate extremes storms. However, it is crucial to note that lower IE time consistently leads to enhanced STH sensitivity (higher magnitude) with temperature.

1hr and 5hr IE times generally represent same extreme storm with shared spatial and temporal center of the storm. The differences in 5hr IE time extreme storm and 1hr IE time extreme storm are primarily observed near the temporal edge of the storm. Specifically, the 5hr IE time extreme storms have a greater or at least same temporal extent as 1hr IE time extreme storms, making the 5hr IE time storms temporally more spread out. Given that the Spatio-Temporal Homogeneity (STH) metric places higher emphasis on precipitation occurring near the spatial and temporal center of the storm, larger STH sensitivity with temperature is observed for temporally smaller storms segregated using 1hr IE time.

3.2 Event Loading and temperature Relations.

In contrast to the sensitivity exhibited by STH, the sensitivity of Event Loading with temperature demonstrates relatively higher consistency across regions around the world. The global median sensitivity of event loading suggests an overall trend of decrease in event loading with rising temperature (median EL sensitivity = -0.76/°C). This negative trend suggests that rising temperature contributes to greater prevalence of front-loaded storm events, a concern as this has implications for flash flooding worldwide. Figure 6a, which presents the geographic variation of EL with temperature, reveals that similar to the STH sensitivity, higher magnitude of EL sensitivity is observed in tropics. While the tropics and southern temperate regions observes increasingly front-loaded storms (negative EL sensitivity), the extreme storms in northern temperate regions tend to get more uniformly loaded, with a slight tendency towards rear-loaded, storms as the temperature increases. It is also interesting to note that regions demonstrating a

408 negative EL sensitivity generally display higher magnitude of sensitivity; whereas regions with
409 positive EL sensitivity exhibit relatively lower magnitude sensitivity with temperature.
410

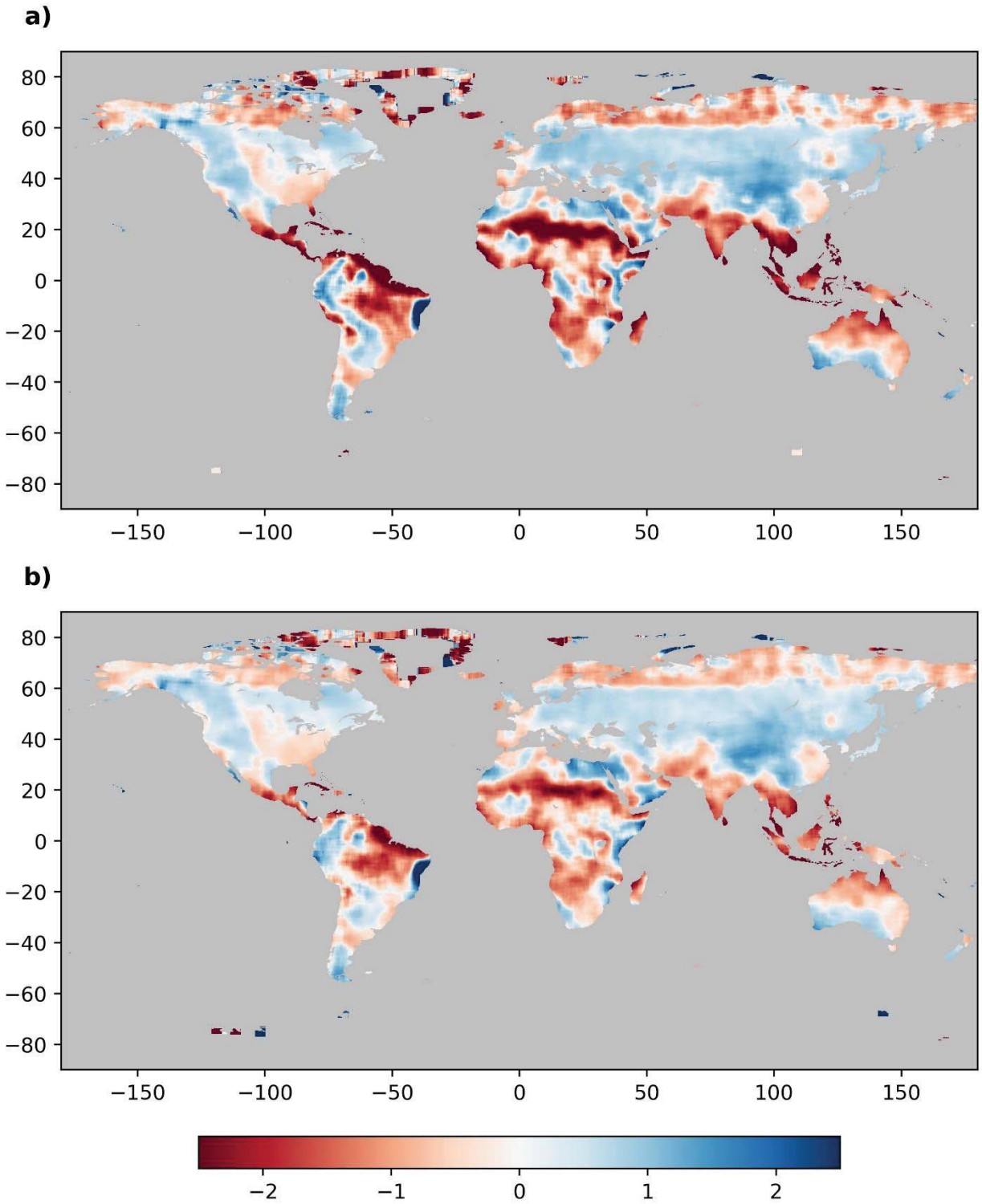

Figure 5 *Results of sensitivity of STH with temperature for two different IE times. a) 4x4° median sensitivity of STH with temperature for 1hr IE time. b) 4x4° median sensitivity of STH with temperature for 5hr IE time.*

Aggregating the results of Figures 6a by the AR5 regions, the distribution of EL sensitivity for different regions are presented as the boxplot in Figure 6b. Among the 33 AR5 regions, 23 regions from ETP* to EAS show consistent negative sensitivity of EL, with SEA (South East Asia), WAF (West Africa) and CAM (Central America) being the three SREX regions with largest negative EL sensitivity. The remaining 9 regions from WAS to MED exhibit positive EL sensitivity with temperature. The three regions showing highest positive EL sensitivity are MED (Mediterranean), CAS (Central Asia) and CNA (Central North America). The intra AR5 region variability in EL sensitivity is lower compared to that of STH sensitivity. Any AR5 region exhibiting negative (positive) median EL sensitivity has negative (positive) EL sensitivity in most AR5 regions. This is also reflected in the fact that only one AR5 region, EAS (East Asia) has overall negligible median EL sensitivity.

Examining both EL sensitivity and STH sensitivity in tandem, it becomes evident that the tropics exhibit negative sensitivities to both EL and STH with increasing temperature. This implies that increasing temperature in tropics results in storms that are more front-loaded, localized, and peakier (localized in terms of both space and time). This trend is noticeably observed in various tropical AR5 regions, including AMZ, CAM, CAR*, SAS, NAU, NEB, SEA, WAF as well as EAF. Beyond the tropics, a similar pattern of more front-loaded and localized storms with increased temperatures is found in the Arctic region (ARC*), the subarctic ALA, NEU (with the EL trend in NEU influenced by Scandinavian countries), arid Sahara (SAH), as well as the temperate SAF and temperate parts of NAU.

Conversely, temperate regions, especially in the northern temperate regions like CEU, CAS, EAS, WAS, and WNA, exhibit positive EL and STH sensitivity to temperature. In these areas, a temperature increase results in storms of increased duration and extent, and more uniformly loaded characteristics, with slight tendencies towards being rear-loaded storms. The temperate regions of North America (CGI, CNA, ENA) and the Mediterranean (MED) experience more localized and peakier, yet uniformly loaded storms (with slight rear-loaded tendencies) as temperature rises. Meanwhile, the temperate regions of Southern America (SSA, WSA) and Australia (SAU) witness storms that grow in temporal extent with rising temperatures but also become more front-loaded.

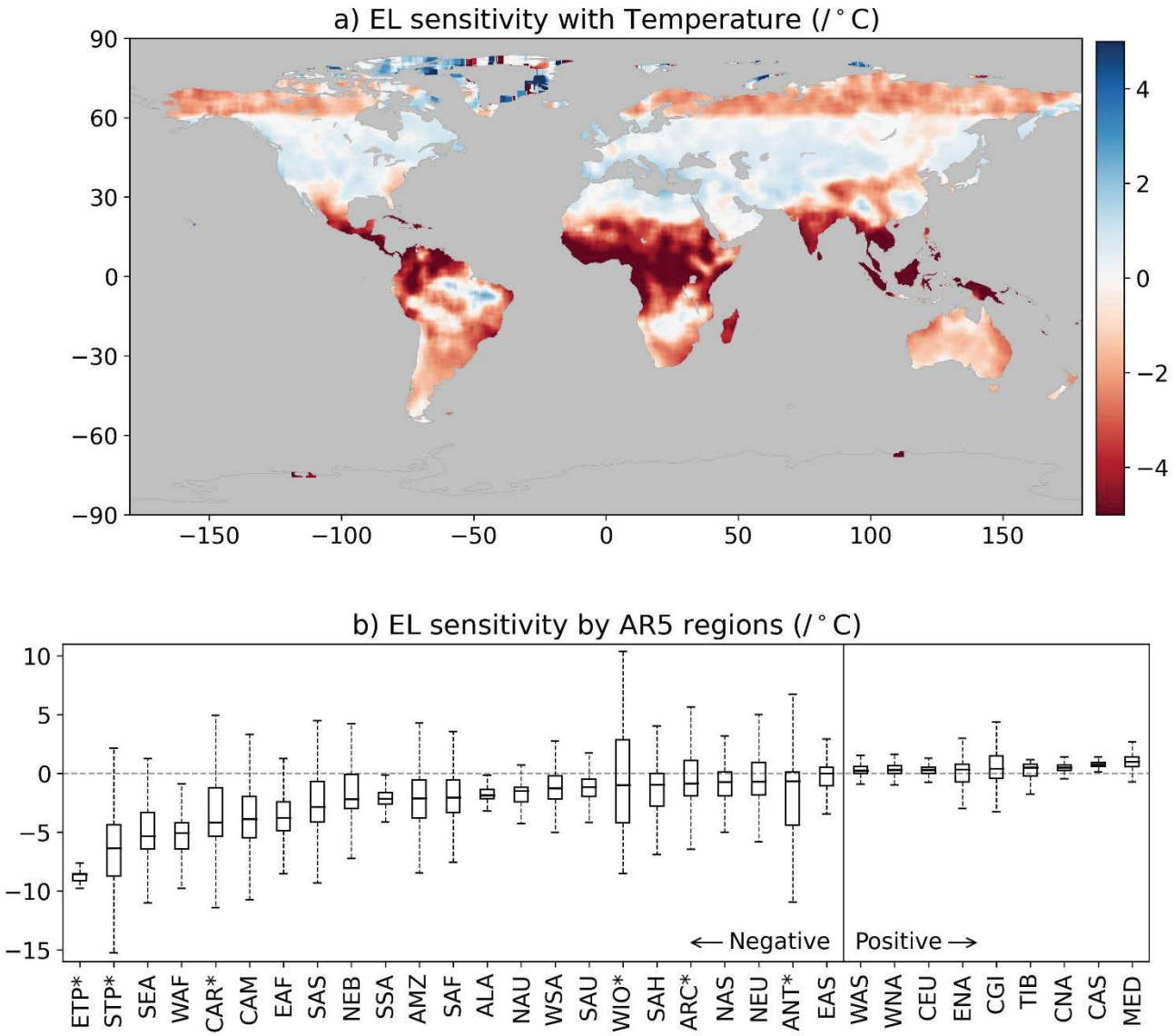

Figure 6 *Results of sensitivity of Event Loading with temperature for 5hr IE time. a) 4°x4° median EL sensitivity with temperature b) Variation in EL sensitivity with temperature for different IPCC AR5 regions.*

3.3 Spatio-Temporal patterns and storm duration.

The findings delineated in previous sections of this study encapsulate trends pertaining to storms of all durations at their location. However, it is imperative to acknowledge that precipitation events inherently exhibit distinct intensity characteristics for different durations. Events of shorter duration (convective) tend to yield higher peak intensity while longer duration events (stratiform) typically display lower peak intensities (Visser et al. 2021). Consequently, intervals marked by higher intensity precipitation within events are poised to manifest steeper

457 spatio-temporal pattern slopes. This dynamic has the potential to instigate more pronounced
458 differentials in both spatio-temporal homogeneity and event loading values for higher intensity
459 and smaller duration events compared to events characterized by lower intensity and longer
460 duration. Therefore, to delve deeper into these trends and discern potential dependencies on
461 storm duration, this section elucidates the variations in spatio-temporal homogeneity and event
462 loading of extreme storms in response to temperature across different storm durations.

463 For a comprehensive analysis, storms at each grid cell are categorized based on their total
464 duration, specifically into bins of 0-3 hours, 3-6 hours, 6-12 hours, 12-24 hours, 24-48 hours, 48-
465 72 hours, and storms exceeding 72 hours. However, this binning approach, while valuable, poses
466 a challenge due to the diminished number of storm events within individual bins at specific cells,
467 rendering them inadequate for robust conclusions. To address this limitation, a solution is
468 implemented by aggregating storms within the 1°x1° neighborhood surrounding each cell. This
469 strategy, akin to the 'trading space for time approach,' capitalizes on the climatic and contextual
470 similarities within the neighborhood of each grid cell. Notably, this 'trading space for time
471 approach' is a recognized method in hydrology and frequently employed in regional flood
472 frequency analysis(Ochoa-Tocachi et al., 2016; R. Singh et al., 2011, 2014).

473 Figure 7 illustrates the median sensitivity of Spatial-Temporal Homogeneity (STH) with
474 temperature across distinct AR5 regions. Three distinct patterns manifest in how STH sensitivity
475 to temperature varies across different storm durations in specific climatic zones the tropics
476 (AMZ, SAS, SEA, NEB, WAF), northern temperate regions (WNA, CNA, ENA, NEU, CEU,
477 MED, NAS, CAS, TIB, EAS, WAS), and southern temperate regions (WSA, SSA, EAF SAF
478 SAU). It is imperative to acknowledge that AR5 regions encompass diverse climate subtypes,
479 and the broad categorization into tropical, temperate, and northern/southern temperate here is a
480 simplification for clarity in comprehending these distinctive patterns.

481 For storms lasting 0-6 hours in the tropics, a negative STH sensitivity is observed,
482 transitioning to a positive sensitivity for 6-12 hour storms (Figure 7a). Subsequently, the
483 sensitivity reverts to negativity for storms spanning 12-48 hours, ultimately diminishing to zero
484 for more extended storm durations. Although not overtly apparent in Figure 7a due to the
485 presentation of median values over larger areas, tropical regions exhibit higher sensitivity
486 magnitudes for shorter-duration storms (3-6hr storms) (Figure S2 in supplementary information
487 presents sensitivity maps across all regions).

In contrast, STH sensitivity for storms in northern temperate regions is consistently positive, reaching its zenith for 12-24 hour storms before converging to zero for multiday storms (Figure 7b & 7c). Southern temperate regions exhibit maximum positive STH sensitivity for storms of 3-6 hours duration, followed by a shift to negative sensitivity for storms lasting multiple days (>12 hours), ultimately converging to zero (Figure 7d). This observed pattern in southern temperate regions is also mirrored in NAU and CAM, which represent a blend of arid and tropical climates, as well as in the arid Sahara (SAH) (Figure 7e).

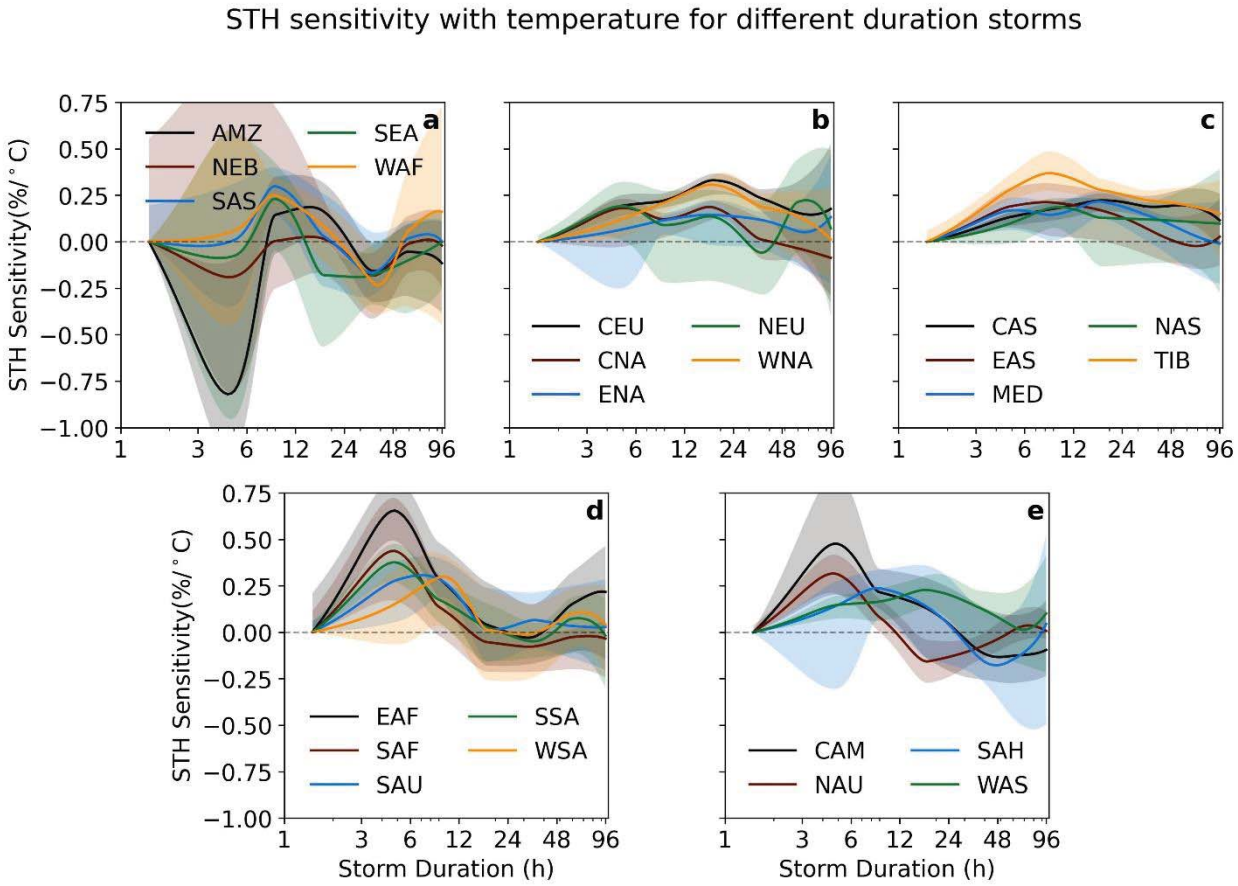

Figure 7 *STH sensitivity with temperature for different duration storms. The plot presents pattern of STH sensitivity change for specific climatic zones a) Tropical AR5 regions AMZ, NEB, SAS, SEA, WAF; b) Northern Temperate AR5 regions CEU, CNA, ENA, NEU, WNA; c) more Northern Temperate AR5 regions CAS, EAS, MED, NAS, TIB; d) Southern Temperate regions EAF, SAF, SAU, SSA, WSA; e) Regions mix of Arid and Tropical Climate NAU, WAS, arid region of SAH and northern Temperate region CAM. The solid lines are spline interpolation to demonstrate the variation and represent median STH sensitivity with temperature for that*

503 *duration while the shaded regions highlight the variation of STH sensitivity between 25th and*
504 *75th quantile.*

505 Figure 8 depicts the median sensitivity of Event Loading (EL) with temperature across
506 diverse AR5 regions. Notably, the sensitivity patterns of EL with temperature are distinctive:
507 regions situated south of 30° N latitude demonstrate a more pronounced negative sensitivity of
508 EL for short-duration storms (Figure 8a, 8d, 8e) with this sensitivity diminishing as the storm
509 duration increases, ultimately converging to zero. In contrast, regions located north of 30° N
510 exhibit the highest positive EL sensitivity for storms lasting 6-12 hours, and longer duration
511 storms show little to no change in EL as temperature varies (Figure 8b, 8c).

512 Irrespective of geographical location, storms worldwide manifest heightened EL
513 sensitivity for shorter duration events, reaching its zenith for storms spanning 6-12 hours, and
514 converging to zero with an increase in storm duration. A noteworthy observation is that storms
515 lasting 0-3 hours and 3-6 hours do not exhibit any discernible change in EL concerning
516 temperature. This phenomenon might be attributed to a potential reduction in the sampling of
517 storms within the 0-3 hour duration range, possibly influenced by the larger interevent time, or
518 linked to the broader temporal domain of the STH metric, which scrutinizes storm behavior from
519 9 hours before the peak to 9 hours after the peak.

520

521 **4. Discussion.**

522 The comprehensive analysis of spatial and temporal characteristics of extreme storms,
523 considering metrics such as Spatial-Temporal Homogeneity (STH) and Event Loading (EL)
524 sensitivity with temperature across various AR5 regions, has revealed nuanced patterns and
525 noteworthy regional variations. These variations are intricately related to the dominant storm
526 type and mechanism in the region as well as moisture availability for the storm duration.

527 Rising temperature in tropical climates results in more non uniform storms, with these
528 storms becoming increasingly spatially and temporally concentrated as well as more front
529 loaded. This tendency could be primarily related to dominance of short duration convective
530 events in the tropical regions. These findings align with location specific analyses, as evidenced
531 by (Long et al., 2021), who observed individual reduction in spatial and temporal scale of
532 extreme storms in humid tropical parts of Eastern China. Similar conclusions were drawn by
533 Wasko and Sharma (2015) while analyzing the temporal patterns of storms in Australia. They

found that storms particularly those in tropical parts of Northern Australia, concentrate in time and become "peakier" in response to increasing temperatures. While studies on storm event loading are limited, our results align with recent research by Visser et al. (2023), which identified a systematic shift toward increased front-loaded temporal patterns, especially in tropical storms, as a response to escalating temperatures.

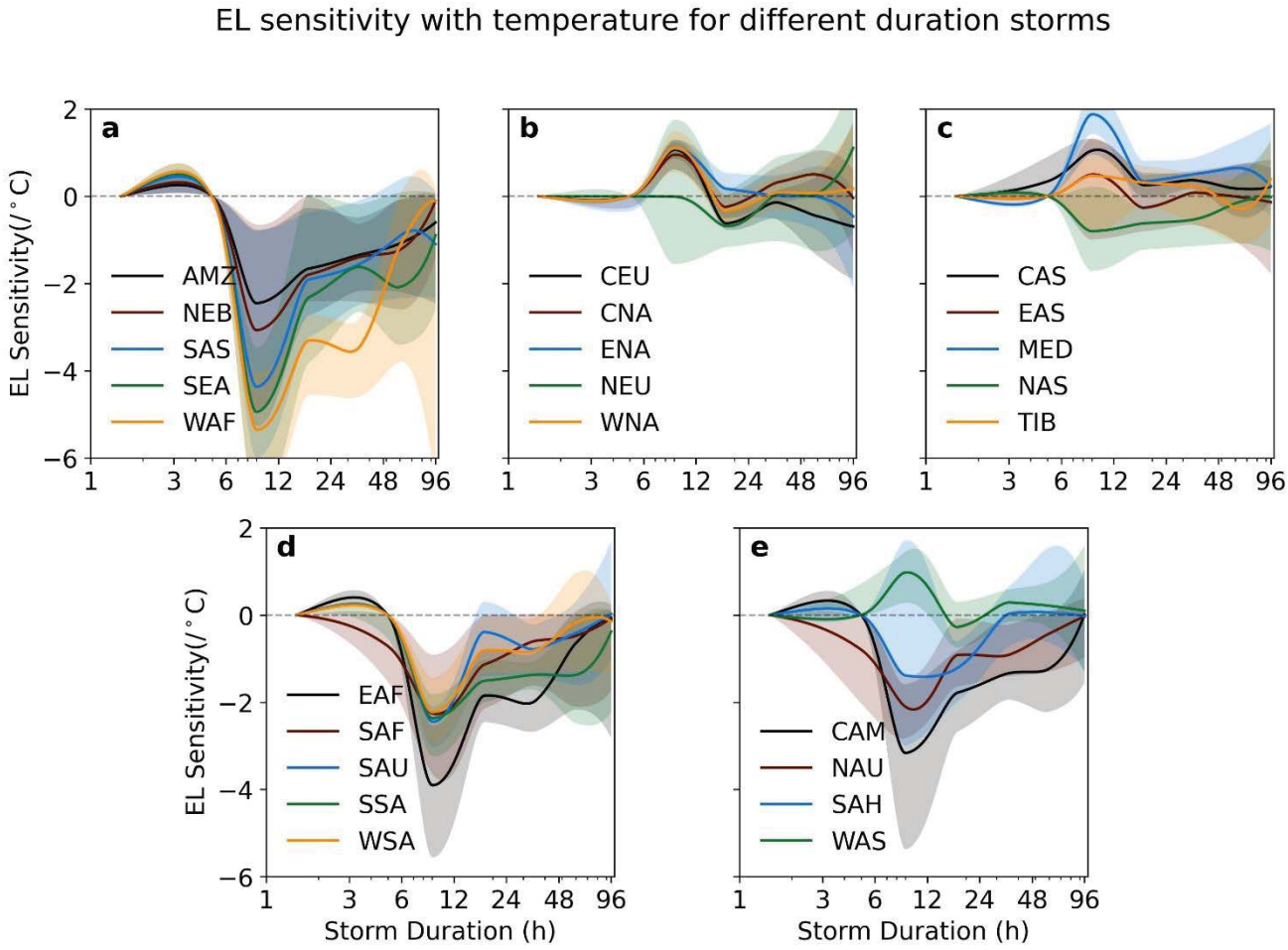

Figure 8 *Similar to Figure 7 but this figure presents EL sensitivity with temperature for different duration storms. The plot presents pattern of EL sensitivity change for specific climatic zones a) Tropical AR5 regions AMZ, NEB, SAS, SEA, WAF; b) Northern Temperate AR5 regions CEU, CNA, ENA, NEU, WNA; c) more Northern Temperate AR5 regions CAS, EAS, MED, NAS, TIB; d) Southern Temperate regions EAF, SAF, SAU, SSA, WSA; e) Regions mix of Arid and Tropical Climate NAU, WAS, arid region of SAH and northern Temperate region CAM. The solid lines are spline interpolation to demonstrate the variation and represent median EL sensitivity with*

548 *temperature for that duration while the shaded regions highlight the variation of EL sensitivity*
549 *between 25th and 75th quantile.*
550
551 Conversely, storms in northern temperate regions exhibit increasing spatio-temporal
552 extent (increasing STH) and more rear-loadedness as temperatures rise. Storms in these higher
553 latitudes tend to be more dependent on low pressure systems and atmospheric rivers than
554 convection; emphasizing the thermodynamic contribution to precipitation over the dynamic
555 contribution (Chan et al., 2016; Lavers & Villarini, 2013; Newell et al., 1992; Z. Yang &
556 Villarini, 2019). These results are in line with the findings of Yang et al. (2023), who utilized
557 EURO-CORDEX initiative and found that extreme events in Germany will become more
558 temporally spread and homogenous in space as temperatures rise in future. The event loading
559 trends are consistent with the findings of (Fadhel et al., 2018), who observed dominance of rear
560 loaded storms in West Yorkshire in North England. A notable exception to these northern
561 temperate regions includes storms in Central and Eastern North America, Mediterranean region,
562 and parts of western Europe. While storms in these regions become increasingly rear loaded with
563 rising temperature but they exhibit a decreasing spatio-temporal extent, becoming more localized
564 and peakier. (Hettiarachchi et al., 2019) had earlier identified a similar temporal intensification
565 pattern for storms in Minneapolis, United States.
566 The variability observed in STH sensitivity across different storm durations can be
567 attributed to the moisture availability for storms of that duration. The marginally negative STH
568 sensitivity noted for short-duration (0-6 hour) storms in the tropics may be associated with
569 sudden, brief convective storms characterized by rapid local atmospheric moisture release. This
570 results in precipitation rates surpassing the increase in atmospheric moisture sustained at that
571 temperature, a phenomenon often evidenced by a super CC scaling of peak intensity and the
572 observed contraction of storm spatial size in short-duration tropical storms (Wasko and Sharma
573 2015; Ghanghas et al. 2023). However, for 6-12 hour duration storms the thermodynamic factor
574 dominate the storm dynamics, leading to increased available atmospheric moisture with rising
575 temperature. This results in intensity scaling at a consistent rate (CC rate) and an increased
576 spatio-temporal extent of the storm. However, as the storm duration further extends beyond 12-
577 24 hour, the locally available moisture becomes limited, possibly depleted, causing a reduction in
578 spatio-temporal extent of the storm again begins to reduce with increasing temperature. This

579 limitation in available moisture is also reflected in the negative STH sensitivity observed for
580 storms in the arid Sahara. In contrast, continuous moisture influx from low-pressure systems and
581 atmospheric rivers serves as a perpetual moisture source for storms in the northern tropics,
582 resulting in a positive STH sensitivity with temperature across all storm durations (Eiras-Barca et
583 al., 2017; Trenberth & Stepaniak, 2003; Yilmaz & Perera, 2015).
584
585 *Implications for future.*

586 Based on the findings of this study, Ghanghas et al. (2023) and ubiquitous peak intensity
587 scaling of 7%/°C, Figure 9 presents the holistic changes in spatio-temporal structure of storm in
588 Indonesia (Figure 9a) and West Coast of America (Figure 9b) due to an estimated 3°C increase
589 in temperature. These locations serve as representatives for anticipated changes in the tropics and
590 northern temperate regions, respectively. It is important to identify the regions with most
591 changes to spatio-temporal structure of storms and understand the nature of these changes
592 because temporal and spatial pattern of precipitation affects the catchment response, impacting
593 streamflow, sediment transport volumes and peaks (Peleg et al., 2020). Furthermore, less
594 uniform distributions of extreme precipitation have been linked to result in higher flood peaks
595 (Hettiarachchi et al., 2018; Nathan et al., 2016). Although flood responses are catchment-specific
596 and contingent on the storm's relative size to the catchment, our results suggest a potential
597 increase in flood peaks, especially in the tropics, as storms become more spatio-temporally
598 concentrated and front-loaded.

599 Spatio-temporal characteristics play a pivotal role in various rainfall-based flood
600 estimation methods employed for design of engineering infrastructure. While these methods
601 often try to incorporate changes in peak intensity for accurate design estimates, they often
602 assume no alteration in the spatial and temporal structure of the storm, potentially leading to
603 inadequacies in future water infrastructure. Design flood models, relying on the spatial and
604 temporal distribution of storms, need to account for more spatio-temporally concentrated and
605 front-loaded storms. While, stochastic design flood estimation approaches would require non-
606 stationary parameters to precisely capture the changes in the spatio-temporal structure of extreme
607 storms. In contrast continuous simulation methods, employing historical rainfall sequences, may
608 fall short of representing future conditions accurately.

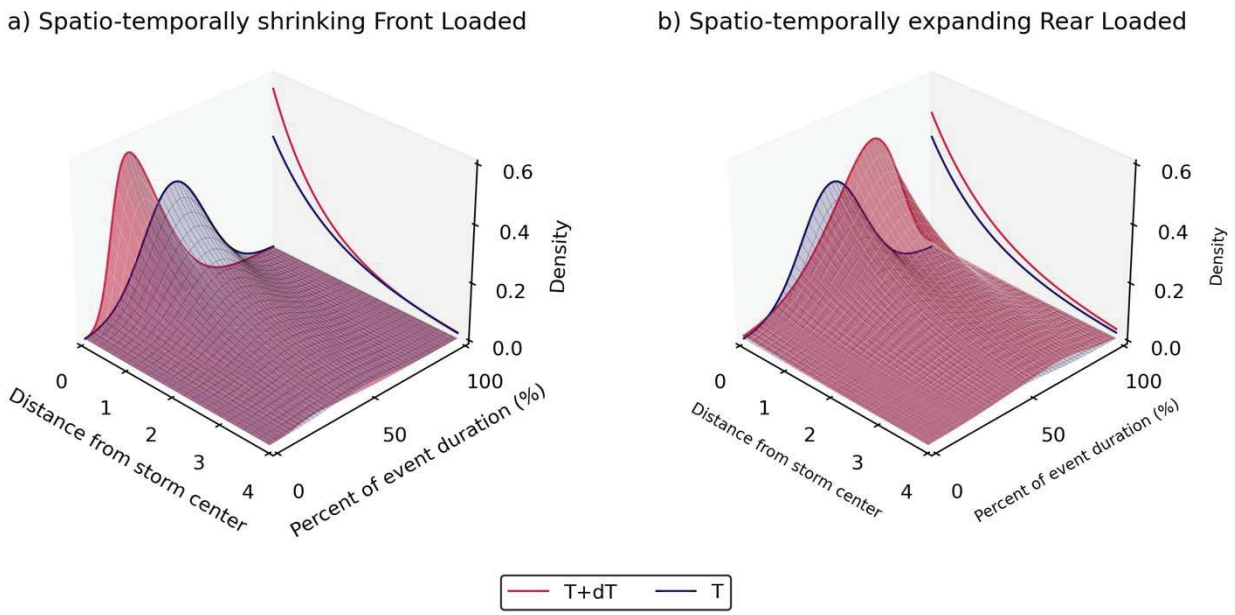

609

610 ***Figure 9*** *Idealized representative precipitation density plot of future spatio-temporal structure of*
611 *storms in a) tropics and in b) northern temperate regions. Red plot and lines represent future*
612 *storms with an estimated 3° C estimated temperature increase, while blue represents base storm*
613 *with uniform precipitation distribution.*

614

615 **Conclusions.**

616 This study introduces a novel metric termed Spatio-Temporal Homogeneity (STH) that can be
617 used to track combined changes in spatio-temporal structure of extreme storms, and their
618 sensitivity to different climate parameters. Investigating the effect of rising temperature on
619 spatio-temporal distribution of precipitation in extreme storms across the globe, the study finds
620 that dominant precipitation mechanism and geographic location play a key role in how storm
621 structure changes. The following conclusions can be drawn from the results presented.

622

623 1. A rise in temperature concentrates precipitation in both space and time resulting in
624 "Smaller and Peakier" storms in Tropics. Furthermore, these storms in tropics also tend
625 to get more and more front-loaded with rising temperature. This trend is also observed in
626 temperate regions where convective storms contributes to majority of extreme
627 precipitation. Conversely, a rise in temperature results in spatio-temporally spread
628 temperate regions.

2. A greater overall prevalence of front loaded storms as temperature rises across the globe. These trends are driven by a significant increase towards front loaded storms in Tropics and Northern temperate regions. On the other hand, extreme storms in southern temperate regions become more uniform or slightly rear loaded in response to increasing temperature.
3. Spatio-temporal structure short durations storms (6–12 hour storms) are generally found to be more sensitive to changes in temperature, with negligible sensitivity for multiday storms.

These findings, combined with the established knowledge that extreme storms intensify in warmer climates, hold substantial implications. In a warming climate, short-duration extreme storms in the tropics will become more intense and concentrated, elevating the risk of severe floods. Furthermore, tropics may experience an increase in flash floods as these intense and concentrated storms would be more front loaded with large proportion of total precipitation occurring before the storm peak.

Acknowledgments

The authors would like to acknowledge the financial support from Purdue University's Ross Fellowship and Lyles School of Civil Engineering Teaching Fellowship. The first author was also partially funded by National Science Foundation (Award #2230092).

Data Availability Statement

All observational datasets and model simulations used in this study are publicly available. ERA5 and ERA5-Land are available from the European Centre for Medium-Range Weather Forecasts' (ECMWF) Copernicus Climate Change Service (C3S) Climate Date Store at https://cds.climate.copernicus.eu/cdsapp#!/dataset/reanalysis-era5-land?tab=overview and https://cds.climate.copernicus.eu/cdsapp#!/dataset/reanalysis-era5-pressure-levels?tab=overview. GPM IMERG data are available at https://gpm.nasa.gov/data.

References

Beck, H. E., Pan, M., Roy, T., Weedon, G. P., Pappenberger, F., Van Dijk, A. I. J. M., Huffman, G. J., Adler, R. F., & Wood, E. F. (2019). Daily evaluation of 26 precipitation datasets using Stage-IV gauge-radar data for the CONUS. *Hydrology and Earth System Sciences*, *23*(1), 207–224. https://doi.org/10.5194/HESS-23-207-2019

Berg, P., Haerter, J. O., Thejll, P., Piani, C., Hagemann, S., & Christensen, J. H. (2009). Seasonal characteristics of the relationship between daily precipitation intensity and surface temperature. *Journal of Geophysical Research Atmospheres*, *114*(18). https://doi.org/10.1029/2009JD012008

Berg, P., Moseley, C., & Haerter, J. O. (2013). Strong increase in convective precipitation in response to higher temperatures. *Nature Geoscience*, *6*(3), 181–185. https://doi.org/10.1038/ngeo1731

Bevacqua, E., Shepherd, T. G., Watson, P. A. G., Sparrow, S., Wallom, D., & Mitchell, D. (2021). Larger Spatial Footprint of Wintertime Total Precipitation Extremes in a Warmer Climate. *Geophysical Research Letters*, *48*(8), e2020GL091990. https://doi.org/10.1029/2020GL091990

Bulovic, N., McIntyre, N., & Johnson, F. (2020). Evaluation of IMERG V05B 30-Min Rainfall Estimates over the High-Elevation Tropical Andes Mountains. *Journal of Hydrometeorology*, *21*(12), 2875–2892. https://doi.org/10.1175/JHM-D-20-0114.1

Chan, S. C., Kendon, E. J., Roberts, N. M., Fowler, H. J., & Blenkinsop, S. (2016). Downturn in scaling of UK extreme rainfall with temperature for future hottest days. *Nature Geoscience*, *9*(1). https://doi.org/10.1038/ngeo2596

Chang, W., Stein, M. L., Wang, J., Kotamarthi, V. R., & Moyer, E. J. (2016). Changes in Spatiotemporal Precipitation Patterns in Changing Climate Conditions. *Journal of Climate*, *29*(23), 8355–8376. https://doi.org/10.1175/JCLI-D-15-0844.1

Chen, Y., Paschalis, A., Kendon, E., Kim, D., & Onof, C. (2021). Changing Spatial Structure of Summer Heavy Rainfall, Using Convection-Permitting Ensemble. *Geophysical Research Letters*, *48*(3), e2020GL090903. https://doi.org/10.1029/2020GL090903

Collins, M., Knutti, R., Arblaster, J., Dufresne, J., Fichefet, T., Friedlingstein, P., Gao, X., Gutowski, W., Johns, T., Krinner, G., Shongwe, M., Tebaldi, C., Weaver, A., & Wehner, M. (2013). Long-term Climate Change: Projections, Commitments and Irreversibility. In: Climate Change 2013: The Physical Science. *Climate Change 2013 the Physical Science Basis: Working Group I Contribution to the Fifth Assessment Report of the Intergovernmental Panel on Climate Change*, *January 2014*.

Eiras-Barca, J., Dominguez, F., Hu, H., Garaboa-Paz, D., & Miguez-Macho, G. (2017). Evaluation of the moisture sources in two extreme landfalling atmospheric river events using an Eulerian WRF tracers tool. *Earth System Dynamics*, *8*(4). https://doi.org/10.5194/esd-8-1247-2017

Emori, S., & Brown, S. J. (2005). Dynamic and thermodynamic changes in mean and extreme precipitation under changed climate. *Geophysical Research Letters*, *32*(17). https://doi.org/10.1029/2005GL023272

Fadhel, S., Rico-Ramirez, M. A., & Han, D. (2018). Sensitivity of peak flow to the change of rainfall temporal pattern due to warmer climate. *Journal of Hydrology*, *560*, 546–559. https://doi.org/10.1016/J.JHYDROL.2018.03.041

Fischer, E. M., & Knutti, R. (2016). Observed heavy precipitation increase confirms theory and early models. *Nature Climate Change*, *6*(11), 986–991. https://doi.org/10.1038/NCLIMATE3110

Fowler, H. J., Lenderink, G., Prein, A. F., Westra, S., Allan, R. P., Ban, N., Barbero, R., Berg, P., Blenkinsop, S., Do, H. X., Guerreiro, S., Haerter, J. O., Kendon, E. J., Lewis, E., Schaer, C., Sharma, A., Villarini, G., Wasko, C., & Zhang, X. (2021). Anthropogenic intensification of short-duration rainfall extremes. In *Nature Reviews Earth and Environment* (Vol. 2, Issue 2). https://doi.org/10.1038/s43017-020-00128-6

Gao, S., & Fang, Z. N. (2019). Investigating hydrologic responses to spatio-temporal characteristics of storms using a Dynamic Moving Storm generator. *Hydrological Processes*, *33*(21), 2729–2744. https://doi.org/10.1002/HYP.13524

Ghanghas, A., Sharma, A., Dey, S., & Merwade, V. (2023). How Is Spatial Homogeneity in Precipitation Extremes Changing Globally? *Geophysical Research Letters*, *50*(16), e2023GL103233. https://doi.org/10.1029/2023GL103233

Guerreiro, S. B., Fowler, H. J., Barbero, R., Westra, S., Lenderink, G., Blenkinsop, S., Lewis, E., & Li, X. F. (2018). Detection of continental-scale intensification of hourly rainfall extremes. In *Nature Climate Change* (Vol. 8, Issue 9). https://doi.org/10.1038/s41558-018-0245-3

Hersbach, H., Bell, B., Berrisford, P., Hirahara, S., Horányi, A., Muñoz-Sabater, J., Nicolas, J., Peubey, C., Radu, R., Schepers, D., Simmons, A., Soci, C., Abdalla, S., Abellan, X., Balsamo, G., Bechtold, P., Biavati, G., Bidlot, J., Bonavita, M., … Thépaut, J.-N. (2020). The ERA5 global reanalysis. *Q J R Meteorol Soc*, *146*, 1999–2049. https://doi.org/10.1002/qj.3803

Hettiarachchi, S., Wasko, C., & Sharma, A. (2018). Increase in flood risk resulting from climate change in a developed urban watershed - The role of storm temporal patterns. *Hydrology and Earth System Sciences*, *22*(3). https://doi.org/10.5194/hess-22-2041-2018

Hettiarachchi, S., Wasko, C., & Sharma, A. (2019). Can antecedent moisture conditions modulate the increase in flood risk due to climate change in urban catchments? *Journal of Hydrology*, *571*, 11–20. https://doi.org/10.1016/J.JHYDROL.2019.01.039

Huffman, G. J., Bolvin, D. T., Braithwaite, D., Hsu, K.-L., Joyce, R. J., Kidd, C., Nelkin, E. J., Sorooshian, S., Stocker, E. F., Tan, J., Wolff, D. B., & Xie, P. (2020). Integrated Multi-satellite Retrievals for the Global Precipitation Measurement (GPM) Mission (IMERG). In V. Levizzani, C. Kidd, D. B. Kirschbaum, C. D. Kummerow, K. Nakamura, & F. J. Turk (Eds.), *Satellite Precipitation Measurement: Volume 1* (pp. 343–353). Springer International Publishing. https://doi.org/10.1007/978-3-030-24568-9_19

Koenker, R., & Bassett, G. (1978). Regression Quantiles. *Econometrica*, *46*(1). https://doi.org/10.2307/1913643

Lau, A., & Behrangi, A. (2022). Understanding Intensity–Duration–Frequency (IDF) Curves Using IMERG Sub-Hourly Precipitation against Dense Gauge Networks. *Remote Sensing*, *14*(19). https://doi.org/10.3390/rs14195032

Lavers, D. A., & Villarini, G. (2013). Atmospheric Rivers and Flooding over the Central United States. *Journal of Climate*, *26*(20), 7829–7836. https://doi.org/10.1175/JCLI-D-13-00212.1

Lenderink, G., & van Meijgaard, E. (2008). Increase in hourly precipitation extremes beyond expectations from temperature changes. *Nature Geoscience*, *1*(8), 511–514. https://doi.org/10.1038/ngeo262

Li, J., Wasko, C., Johnson, F., Evans, J. P., & Sharma, A. (2018). Can Regional Climate Modeling Capture the Observed Changes in Spatial Organization of Extreme Storms at Higher Temperatures? *Geophysical Research Letters*, *45*(9), 4475–4484. https://doi.org/10.1029/2018GL077716

Libertino, A., Sharma, A., Lakshmi, V., & Claps, P. (2016). A global assessment of the timing of extreme rainfall from TRMM and GPM for improving hydrologic design. *Environmental Research Letters*, *11*(5). https://doi.org/10.1088/1748-9326/11/5/054003

Lochbihler, K., Lenderink, G., & Siebesma, A. P. (2017). The spatial extent of rainfall events and its relation to precipitation scaling. *Geophysical Research Letters*, *44*(16), 8629–8636. https://doi.org/10.1002/2017GL074857

Long, K., Wang, D., Wang, G., Zhu, J., Wang, S., & Xie, S. (2021). Higher Temperature Enhances Spatiotemporal Concentration of Rainfall. *Journal of Hydrometeorology*, *22*(12). https://doi.org/10.1175/jhm-d-21-0034.1

Masson-Delmotte, V., Zhai, P., Pirani, A., Connors, S. L., Péan, C., Berger, S., Caud, N., Chen, Y., Goldfarb, L., Gomis, M. I., Huang, M., Leitzell, K., Lonnoy, E., Matthews, J. B. R., Maycock, T. K., Waterfield, T., Yelekçi, O., Yu, R., Zhou, B., & (eds.). (2021). IPCC, 2021: Climate Change 2021: The Physical Science Basis. In *Cambridge University Press. In Press.* https://doi.org/10.1017/9781009157896

Matte, D., Christensen, J. H., & Ozturk, T. (2022). Spatial extent of precipitation events: when big is getting bigger. *Climate Dynamics*, *58*(5), 1861–1875. https://doi.org/10.1007/s00382-021-05998-0

Mishra, V., Wallace, J. M., & Lettenmaier, D. P. (2012). Relationship between hourly extreme precipitation and local air temperature in the United States. *Geophysical Research Letters*, *39*(16). https://doi.org/https://doi.org/10.1029/2012GL052790

Muñoz-Sabater, J., Dutra, E., Agust\'{\i}-Panareda, A., Albergel, C., Arduini, G., Balsamo, G., Boussetta, S., Choulga, M., Harrigan, S., Hersbach, H., Martens, B., Miralles, D. G., Piles, M., Rodr\'{\i}guez-Fernández, N. J., Zsoter, E., Buontempo, C., & Thépaut, J.-N. (2021). ERA5-Land: a state-of-the-art global reanalysis dataset for land applications. *Earth System Science Data*, *13*(9), 4349–4383. https://doi.org/10.5194/essd-13-4349-2021

Nathan, R., Stephens, D., Smith, M., Jordan, P., Scorah, M., Shepherd, D., Hill, P., & Syme, B. (2016). Impact of natural variability on design flood flows and levels. *37th Hydrology and Water Resources Symposium 2016: Water, Infrastructure and the Environment, HWRS 2016*, *2016-November*.

Newell, R. E., Newell, N. E., Zhu, Y., & Scott, C. (1992). Tropospheric rivers? – A pilot study. *Geophysical Research Letters*, *19*(24), 2401–2404. https://doi.org/10.1029/92GL02916

Ochoa-Tocachi, B. F., Buytaert, W., De Bièvre, B., Célleri, R., Crespo, P., Villacís, M., Llerena, C. A., Acosta, L., Villazón, M., Guallpa, M., Gil-Ríos, J., Fuentes, P., Olaya, D., Viñas, P., Rojas, G., & Arias, S. (2016). Impacts of land use on the hydrological response of tropical Andean catchments. *Hydrological Processes*, *30*(22). https://doi.org/10.1002/hyp.10980

Ogden, F. L., & Julien, P. Y. (1993). Runoff Sensitivity to Temporal and Spatial Rainfall Variability at Runoff Plane and Small Basin Scales. *WATER RESOURCES RESEARCH*, *29*(8), 2589–2597. https://doi.org/10.1029/93WR00924

Peleg, N., Marra, F., Fatichi, S., Molnar, P., Morin, E., Sharma, A., & Burlando, P. (2018). Intensification of Convective Rain Cells at Warmer Temperatures Observed from High-Resolution Weather Radar Data. *Journal of Hydrometeorology*, *19*(4), 715–726. https://doi.org/10.1175/JHM-D-17-0158.1

792 Peleg, N., Skinner, C., Fatichi, S., & Molnar, P. (2020). Temperature effects on the spatial
793 structure of heavy rainfall modify catchment hydro-morphological response. *Earth Surface*
794 *Dynamics*, *8*(1). https://doi.org/10.5194/esurf-8-17-2020
795 Seneviratne, S. I., Nicholls, N., Easterling, D., Goodess, C. M., Kanae, S., Kossin, J., Luo, Y.,
796 Marengo, J., Mc Innes, K., Rahimi, M., Reichstein, M., Sorteberg, A., Vera, C., Zhang, X.,
797 Rusticucci, M., Semenov, V., Alexander, L. V., Allen, S., Benito, G., … Zwiers, F. W.
798 (2012). Changes in climate extremes and their impacts on the natural physical environment.
799 In *Managing the Risks of Extreme Events and Disasters to Advance Climate Change*
800 *Adaptation: Special Report of the Intergovernmental Panel on Climate Change* (Vol.
801 9781107025066). https://doi.org/10.1017/CBO9781139177245.006
802 Shah, S. M. S., O'Connell, P. E., & Hosking, J. R. M. (1996). Modelling the effects of spatial
803 variability in rainfall on catchment response. 2. Experiments with distributed and lumped
804 models. *Journal of Hydrology*, *175*(1–4), 89–111. https://doi.org/10.1016/S0022-
805 1694(96)80007-2
806 Sharma, A., Wasko, C., & Lettenmaier, D. P. (2018). If Precipitation Extremes Are Increasing,
807 Why Aren't Floods? *Water Resources Research*, *54*(11), 8545–8551.
808 https://doi.org/10.1029/2018WR023749
809 Singh, R., van Werkhoven, K., & Wagener, T. (2014). Hydrological impacts of climate change
810 in gauged and ungauged watersheds of the Olifants basin: a trading-space-for-time
811 approach. *Hydrological Sciences Journal*, *59*(1).
812 https://doi.org/10.1080/02626667.2013.819431
813 Singh, R., Wagener, T., Van Werkhoven, K., Mann, M. E., & Crane, R. (2011). A trading-space-
814 for-time approach to probabilistic continuous streamflow predictions in a changing climate-
815 accounting for changing watershed behavior. *Hydrology and Earth System Sciences*, *15*(11).
816 https://doi.org/10.5194/hess-15-3591-2011
817 Singh, V. P. (1997). EFFECT OF SPATIAL AND TEMPORAL VARIABILITY IN
818 RAINFALL AND WATERSHED CHARACTERISTICS ON STREAM FLOW
819 HYDROGRAPH. *Ltd. Hydrol. Process*, *11*, 1649–1669.
820 https://doi.org/10.1002/(SICI)1099-1085(19971015)11:12
821 Sungmin, O., Foelsche, U., Kirchengast, G., Fuchsberger, J., Tan, J., & Petersen, W. A. (2017).
822 Evaluation of GPM IMERG Early, Late, and Final rainfall estimates using WegenerNet
823 gauge data in southeastern Austria. *Hydrology and Earth System Sciences*, *21*(12).
824 https://doi.org/10.5194/hess-21-6559-2017
825 Tan, J., Petersen, W. A., Kirchengast, G., Goodrich, D. C., & Wolff, D. B. (2018). Evaluation of
826 global precipitation measurement rainfall estimates against three dense gauge networks.
827 *Journal of Hydrometeorology*, *19*(3). https://doi.org/10.1175/JHM-D-17-0174.1
828 Tang, G., Clark, M. P., Papalexiou, S. M., Ma, Z., & Hong, Y. (2020). Have satellite
829 precipitation products improved over last two decades? A comprehensive comparison of
830 GPM IMERG with nine satellite and reanalysis datasets. *Remote Sensing of Environment*,
831 *240*, 111697. https://doi.org/10.1016/J.RSE.2020.111697
832 Trenberth, K. E., & Stepaniak, D. P. (2003). Covariability of components of poleward
833 atmospheric energy transports on seasonal and interannual timescales. *Journal of Climate*,
834 *16*(22). https://doi.org/10.1175/1520-0442(2003)016<3691:COCOPA>2.0.CO;2
835 Visser, J. B., Wasko, C., Sharma, A., & Nathan, R. (2020). Resolving Inconsistencies in Extreme
836 Precipitation-Temperature Sensitivities. *Geophysical Research Letters*, *47*(18),
837 e2020GL089723. https://doi.org/https://doi.org/10.1029/2020GL089723

838 Visser, J. B., Wasko, C., Sharma, A., & Nathan, R. (2021). Eliminating the "Hook" in
839 Precipitation–Temperature Scaling. *Journal of Climate*, *34*(23), 9535–9549.
840 https://doi.org/10.1175/JCLI-D-21-0292.1
841 Visser, J., Wasko, C., Sharma, A., & Nathan, R. (2023). Changing storm temporal patterns with
842 increasing temperatures across Australia. *Journal of Climate*, *1*(aop), 1–26.
843 https://doi.org/10.1175/JCLI-D-22-0694.1
844 Wang, G., Wang, D., Trenberth, K. E., Erfanian, A., Yu, M., Bosilovich, M. G., & Parr, D. T.
845 (2017). The peak structure and future changes of the relationships between extreme
846 precipitation and temperature. *Nature Climate Change 2017 7:4*, *7*(4), 268–274.
847 https://doi.org/10.1038/nclimate3239
848 Wasko, C., & Nathan, R. (2019). Influence of changes in rainfall and soil moisture on trends in
849 flooding. *Journal of Hydrology*, *575*, 432–441.
850 https://doi.org/10.1016/J.JHYDROL.2019.05.054
851 Wasko, C., & Sharma, A. (2014). Quantile regression for investigating scaling of extreme
852 precipitation with temperature. *Water Resources Research*, *50*(4), 3608–3614.
853 https://doi.org/https://doi.org/10.1002/2013WR015194
854 Wasko, C., & Sharma, A. (2015). Steeper temporal distribution of rain intensity at higher
855 temperatures within Australian storms. *Nature Geoscience 2014 8:7*, *8*(7), 527–529.
856 https://doi.org/10.1038/ngeo2456
857 Wasko, C., Sharma, A., & Johnson, F. (2015). Does storm duration modulate the extreme
858 precipitation-temperature scaling relationship? Geophysical Research Letters, 42(20).
859 https://doi.org/10.1002/2015GL066274
860 Wasko, C., Sharma, A., & Westra, S. (2016). Reduced spatial extent of extreme storms at higher
861 temperatures. *Geophysical Research Letters*, *43*(8), 4026–4032.
862 https://doi.org/10.1002/2016GL068509
863 Wasko, C., Westra, S., Nathan, R., Pepler, A., Raupach, T., Dowdy, A., Johnson, F., Ho, M.,
864 McInnes, K., Jakob, D., Evans, J., Villarini, G., & Fowler, H. (2023). A systematic review
865 of climate change science relevant to Australian design flood estimation. *Hydrol. Earth*
866 *Syst. Sci. Discuss.*, *2023*, 1–48. https://doi.org/10.5194/hess-2023-232
867 Wati, T., Hadi, T. W., Sopaheluwakan, A., & Hutasoit, L. M. (2022). Statistics of the
868 Performance of Gridded Precipitation Datasets in Indonesia. *Advances in Meteorology*,
869 *2022*. https://doi.org/10.1155/2022/7995761
870 Westra, S., Fowler, H. J., Evans, J. P., Alexander, L. V, Berg, P., Johnson, F., Kendon, E. J.,
871 Lenderink, G., & Roberts, N. M. (2014). Future changes to the intensity and frequency of
872 short-duration extreme rainfall. *Reviews of Geophysics*, *52*(3), 522–555.
873 https://doi.org/10.1002/2014RG000464
874 Yang, L., Franzke, C. L. E., & Duan, W. (2023). Evaluation and projections of extreme
875 precipitation using a spatial extremes framework. *International Journal of Climatology*,
876 *43*(7). https://doi.org/10.1002/joc.8038
877 Yang, Z., & Villarini, G. (2019). Examining the capability of reanalyses in capturing the
878 temporal clustering of heavy precipitation across Europe. *Climate Dynamics*, *53*(3–4),
879 1845–1857. https://doi.org/10.1007/S00382-019-04742-Z/FIGURES/6
880 Yilmaz, A. G., & Perera, B. J. C. (2015). Spatiotemporal Trend Analysis of Extreme Rainfall
881 Events in Victoria, Australia. *Water Resources Management*, *29*(12).
882 https://doi.org/10.1007/s11269-015-1070-3
883

884 ## Figure Captions

885

886 **Figure 1** Precipitation distribution of an extreme storm in space and time (3D surfaces) and
887 individual distribution in space or time (lines) on the 2D projected planes, for conceptual
888 precipitation events of equal duration. Blue surface and lines represent base storm occurring at a
889 cooler temperature, Red surface and lines represent intensified storm occurring at a warmer
890 temperature. a) Traditional temporal intensification with spatial distribution of precipitation
891 increasing proportionately to increase in peak precipitation. b) Spatial Concentration of
892 precipitation towards the spatial center of the storm, no temporal intensification/concentration. c)
893 Temporal intensification along with spatial concentration of the storm, storm concentrating in
894 both space and time. d) Temporal and spatial concentration of the storm along with a lateral shift
895 in spatio-temporal distribution of precipitation.

896

897 **Figure 2.** a) Methodology of STH. As more cells in space and time are included, the red, blue
898 and grey surface show the changes in accumulated weighted precipitation average (AcP) for
899 storm precipitating only at one grid cell and just one time step, original storm to be analyzed, and
900 storm precipitating with same intensity across all grid cells and all-time steps in the space time
901 kernel respectively. b) and c) Methodology of event loading. Purple surface presents the
902 precipitation distribution of original storm to be analyzed and green surface presents the
903 precipitation distribution of rising limb mirrored storm.

904

905 **Figure 3.** Thirty three regions used by Intergovernmental Panel on Climate Change (IPCC)'s
906 Fifth Assessment Report (AR5;(Seneviratne et al., 2012)). The 33 regions comprise of 26 Special
907 Report on Climate Extremes (SREX) regions and 7 non-SREX regions (marked by *). Here,
908 ALA: Alaska/N.W. Canada, AMZ: Amazon, CAM: Central America/Mexico, CAR*: Caribbean,
909 CAS : Central Asia, CEU: Central Europe, CGI: Canada/Greenland/Iceland, CNA: Central
910 North America, EAF: East Africa, EAS: East Asia, ENA: East North America, MED: South
911 Europe/Mediterranean, NAS: North Asia, NAU: North Australia, NEB: North-East Brazil, NEU:
912 North Europe, SAF: Southern Africa, SAH: Sahara, SAS: South Asia, SAU: South
913 Australia/New Zealand, SEA: South East Asia, SSA: Southeastern South America, TIB: Tibetan

914 Plateau, WAF: Western Africa, WAS: West Asia, WNA: West North America, WSA: West
915 Coast South America, ANT*: Antarctica, ARC*: Arctic, NTP* Pacific Islands region, STP*:
916 Southern Tropical Pacific, ETP*: Pacific Islands region, WIO*: West Indian Ocean.

917

918 **Figure 4** Results of sensitivity of STH with temperature for 5hr IE time. A) 4x4° median STH
919 sensitivity with temperature b) Variation in STH sensitivity with temperature for different IPCC
920 AR5 regions.

921

922 **Figure 5** Results of sensitivity of STH with temperature for two different IE times. a) 4x4°
923 median sensitivity of STH with temperature for 1hr IE time. b) 4x4° median sensitivity of STH
924 with temperature for 5hr IE time.

925

926 **Figure 6** Results of sensitivity of Event Loading with temperature for 5hr IE time. a) 4°x4°
927 median EL sensitivity with temperature b) Variation in EL sensitivity with temperature for
928 different IPCC AR5 regions.

929

930 **Figure 7** STH sensitivity with temperature for different duration storms. The plot presents
931 pattern of STH sensitivity change for specific climatic zones a) Tropical AR5 regions AMZ,
932 NEB, SAS, SEA, WAF; b) Northern Temperate AR5 regions CEU, CNA, ENA, NEU, WNA; c)
933 more Northern Temperate AR5 regions CAS, EAS, MED, NAS, TIB; d) Southern Temperate
934 regions EAF, SAF, SAU, SSA, WSA; e) Regions mix of Arid and Tropical Climate NAU, WAS,
935 arid region of SAH and northern Temperate region CAM. The solid lines are spline interpolation
936 to demonstrate the variation and represent median STH sensitivity with temperature for that
937 duration while the shaded regions highlight the variation of STH sensitivity between 25^{th} and
938 75^{th} quantile.

939

940 **Figure 8** Similar to Figure 7 but this figure presents EL sensitivity with temperature for different
941 duration storms. The plot presents pattern of EL sensitivity change for specific climatic zones a)
942 Tropical AR5 regions AMZ, NEB, SAS, SEA, WAF; b) Northern Temperate AR5 regions CEU,
943 CNA, ENA, NEU, WNA; c) more Northern Temperate AR5 regions CAS, EAS, MED, NAS,

944 TIB; d) Southern Temperate regions EAF, SAF, SAU, SSA, WSA; e) Regions mix of Arid and
945 Tropical Climate NAU, WAS, arid region of SAH and northern Temperate region CAM. The
946 solid lines are spline interpolation to demonstrate the variation and represent median EL
947 sensitivity with temperature for that duration while the shaded regions highlight the variation of
948 EL sensitivity between 25^{th} and 75^{th} quantile.
949
950 **Figure 9** Idealized representative precipitation density plot of future spatio-temporal structure of
951 storms in a) tropics and in b) northern temperate regions. Red plot and lines represent future
952 storms with an estimated 3° C estimated temperature increase, while blue represents base storm
953 with uniform precipitation distribution.

Figure 1.

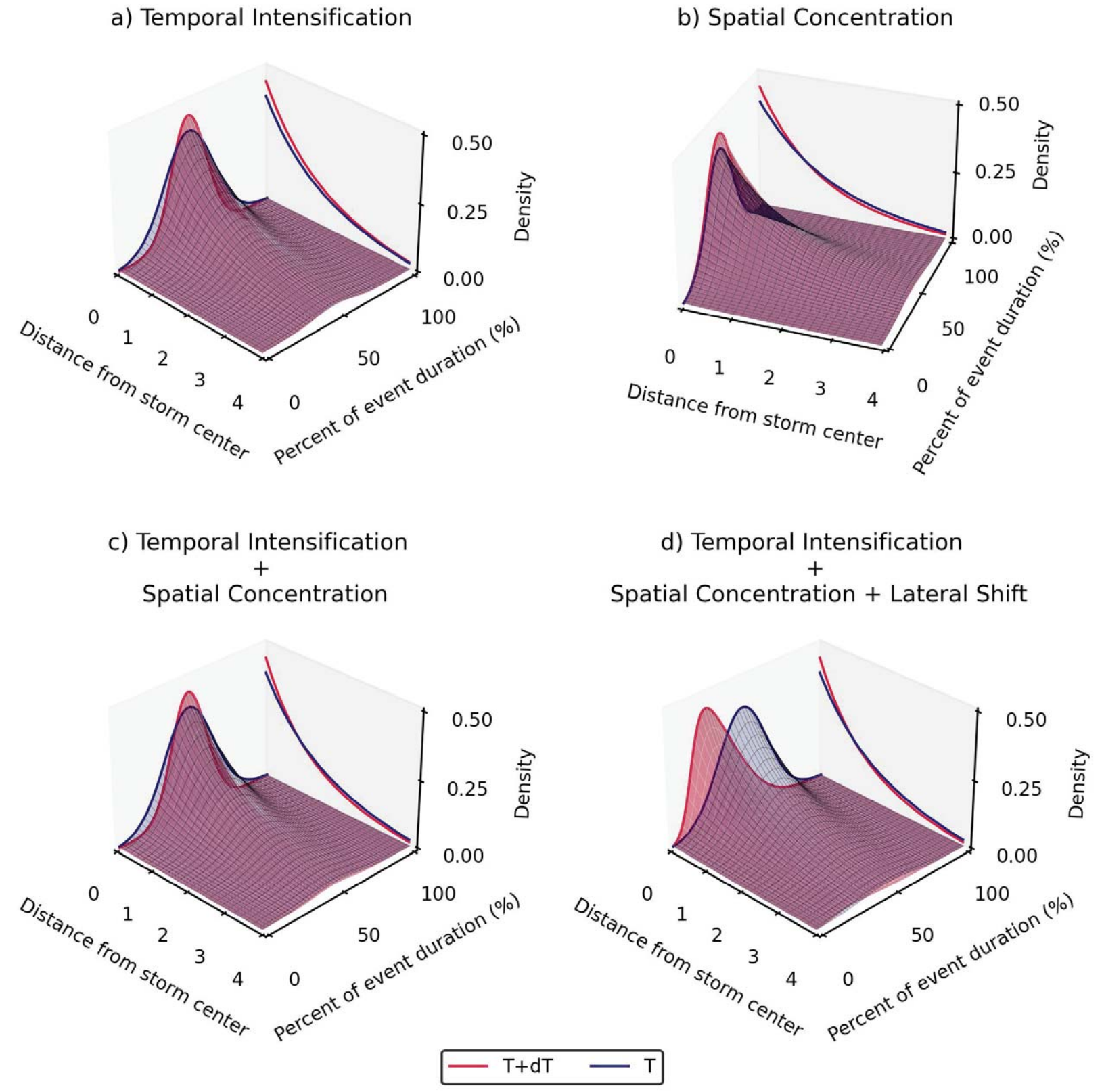
a) Temporal Intensification
b) Spatial Concentration
c) Temporal Intensification
+
Spatial Concentration
d) Temporal Intensification
+
Spatial Concentration + Lateral Shift
Density
0.50
0.25
0.00
Distance from storm center
0
1
2
3
4
Percent of event duration (%)
0
50
100
T+dT
T

Figure 2.

a) STH Methodology

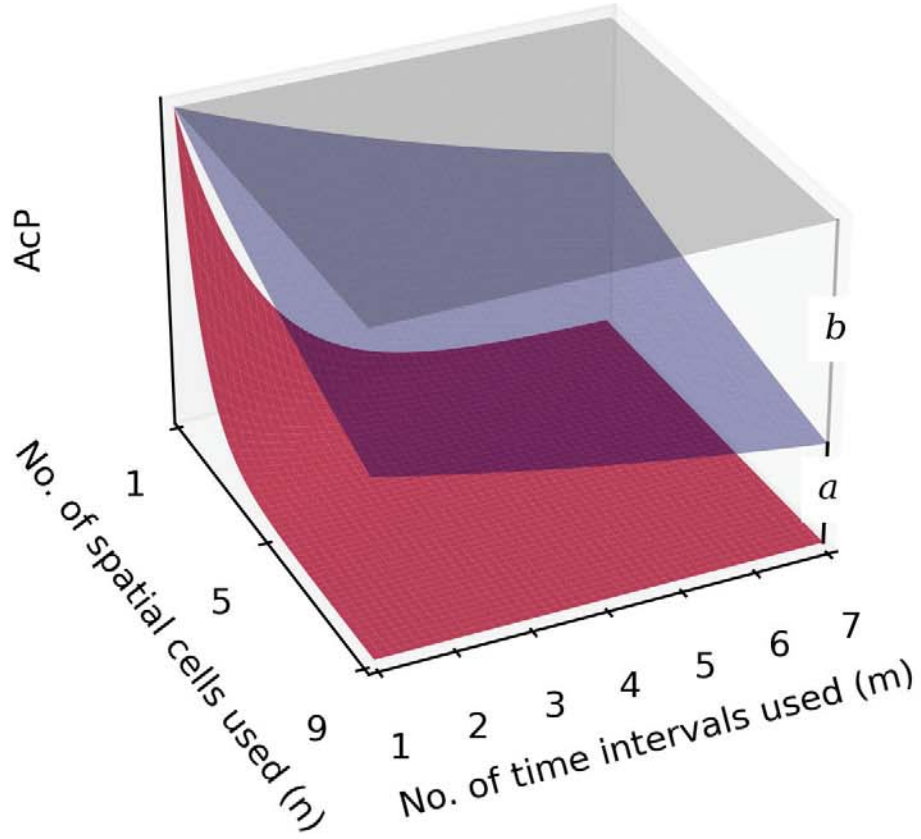

b) Front Loaded Storm

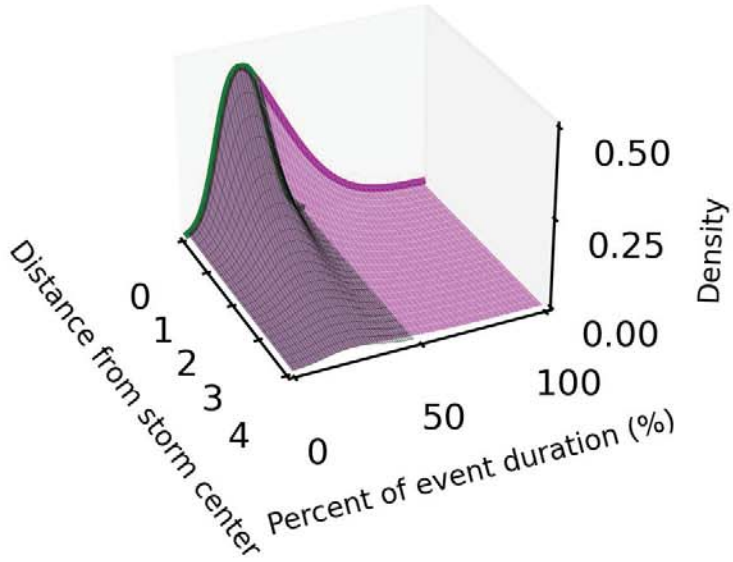

c) Rear Loaded Storm

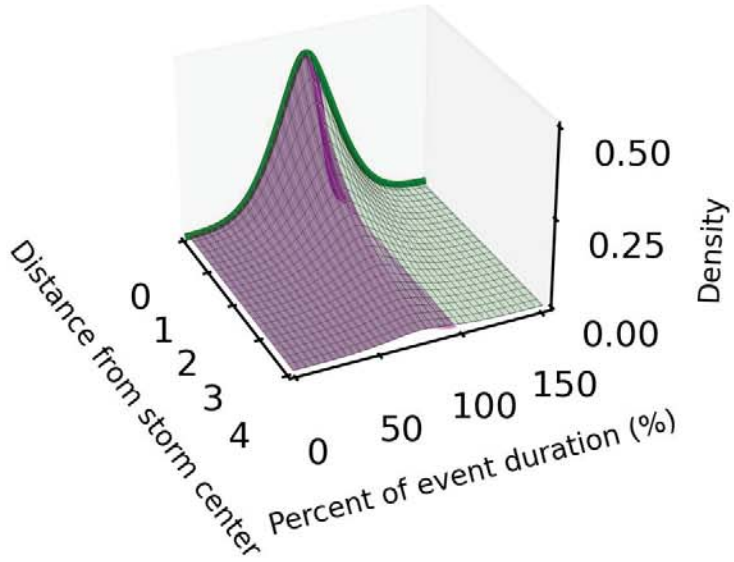

Original Storm Rising Limb Mirrored Storm

Figure 3.

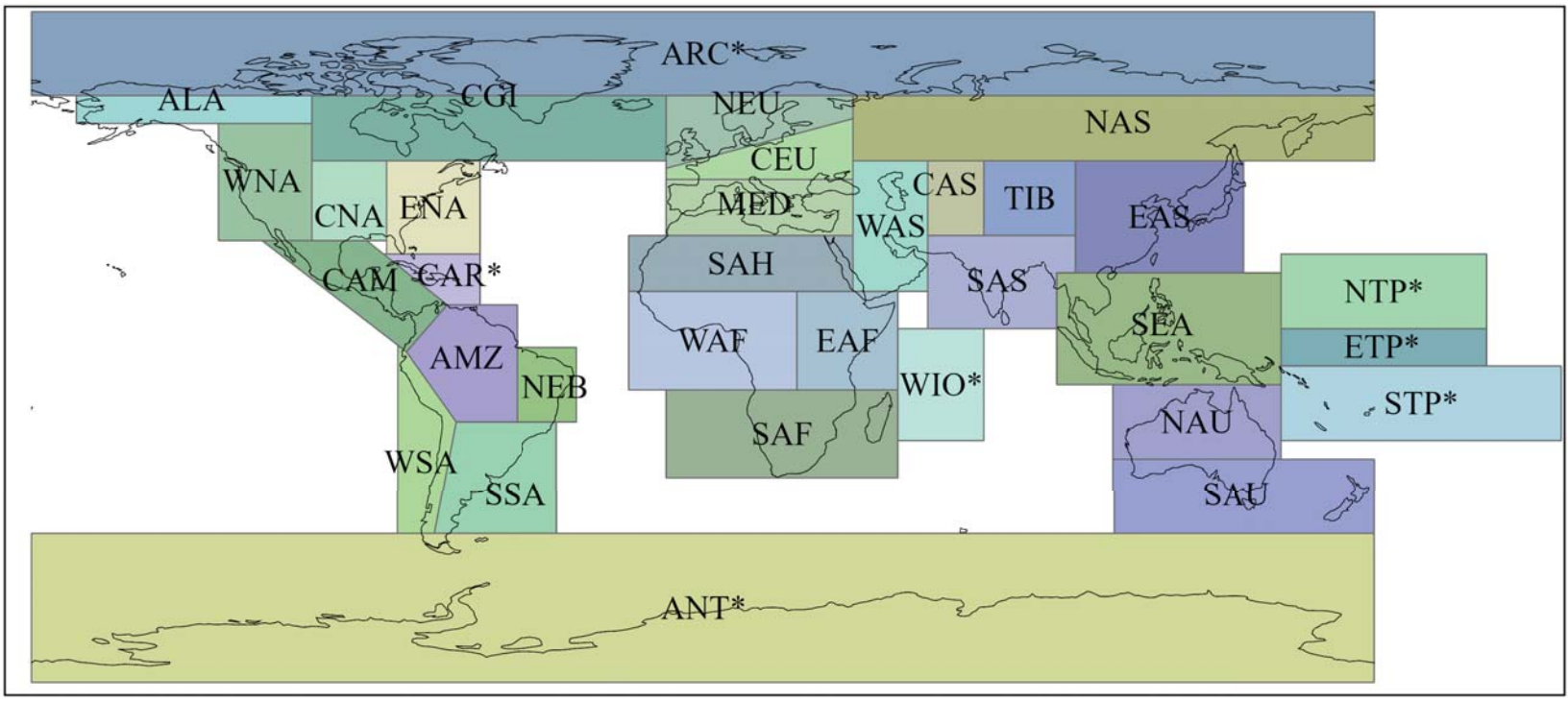
ARC*
ALA
CGI
NEU
NAS
CEU
WNA
CAS
TIB
CNA
ENA
MED
WAS
EAS
SAH
CAM
CAR*
SAS
NTP*
SEA
WAF
EAF
ETP*
AMZ
WIO*
NEB
STP*
SAF
NAU
WSA
SSA
SAU
ANT*

Figure 4.

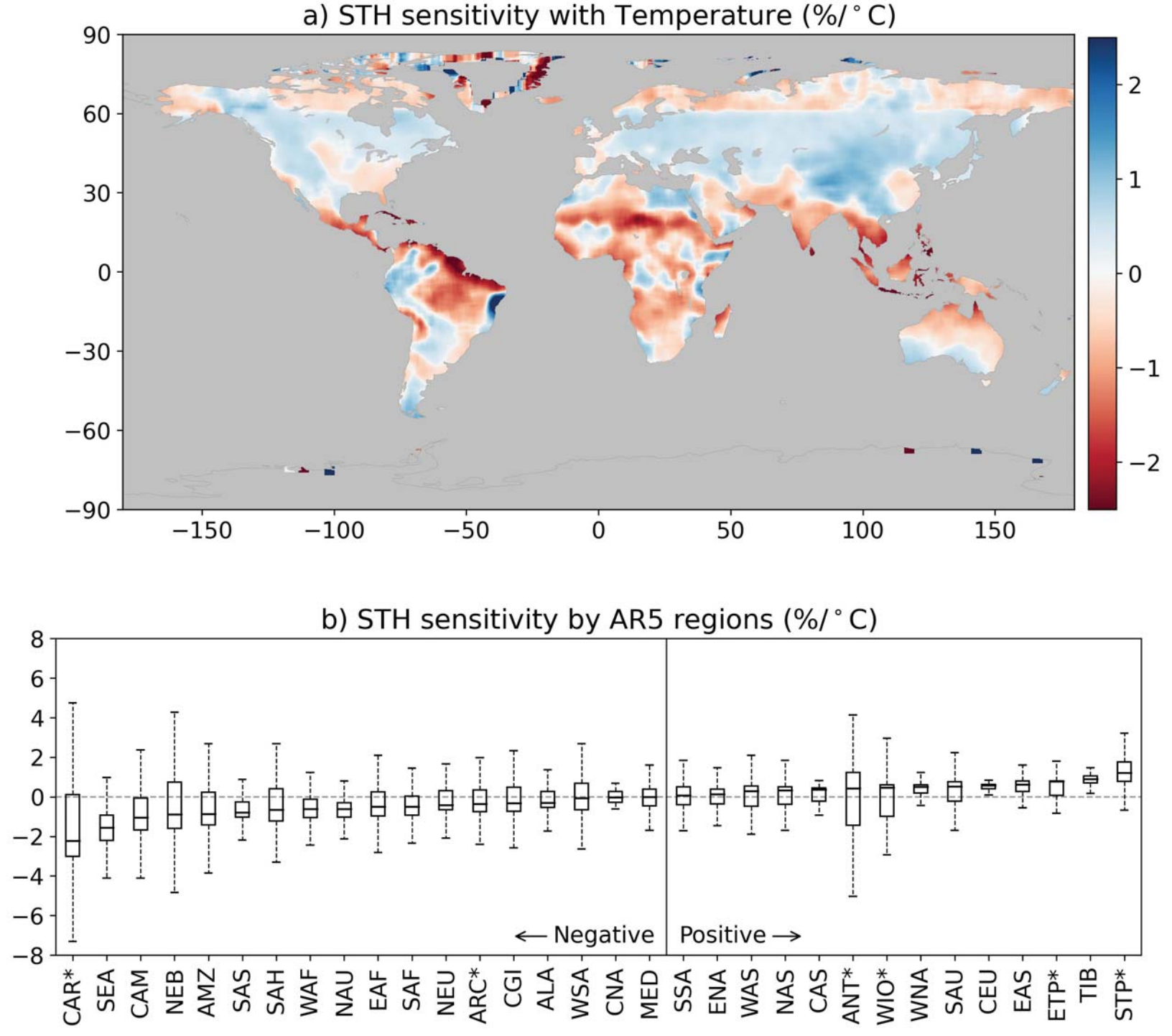
a) STH sensitivity with Temperature (%/°C)
90
60
30
0
−30
−60
−90
−150
−100
−50
0
50
100
150
2
1
0
−1
−2
b) STH sensitivity by AR5 regions (%/°C)
8
6
4
2
0
−2
−4
−6
−8
← Negative
Positive →
CAR*
SEA
CAM
NEB
AMZ
SAS
SAH
WAF
NAU
EAF
SAF
NEU
ARC*
CGI
ALA
WSA
CNA
MED
SSA
ENA
WAS
NAS
CAS
ANT*
WIO*
WNA
SAU
CEU
EAS
ETP*
TIB
STP*

Figure 5.

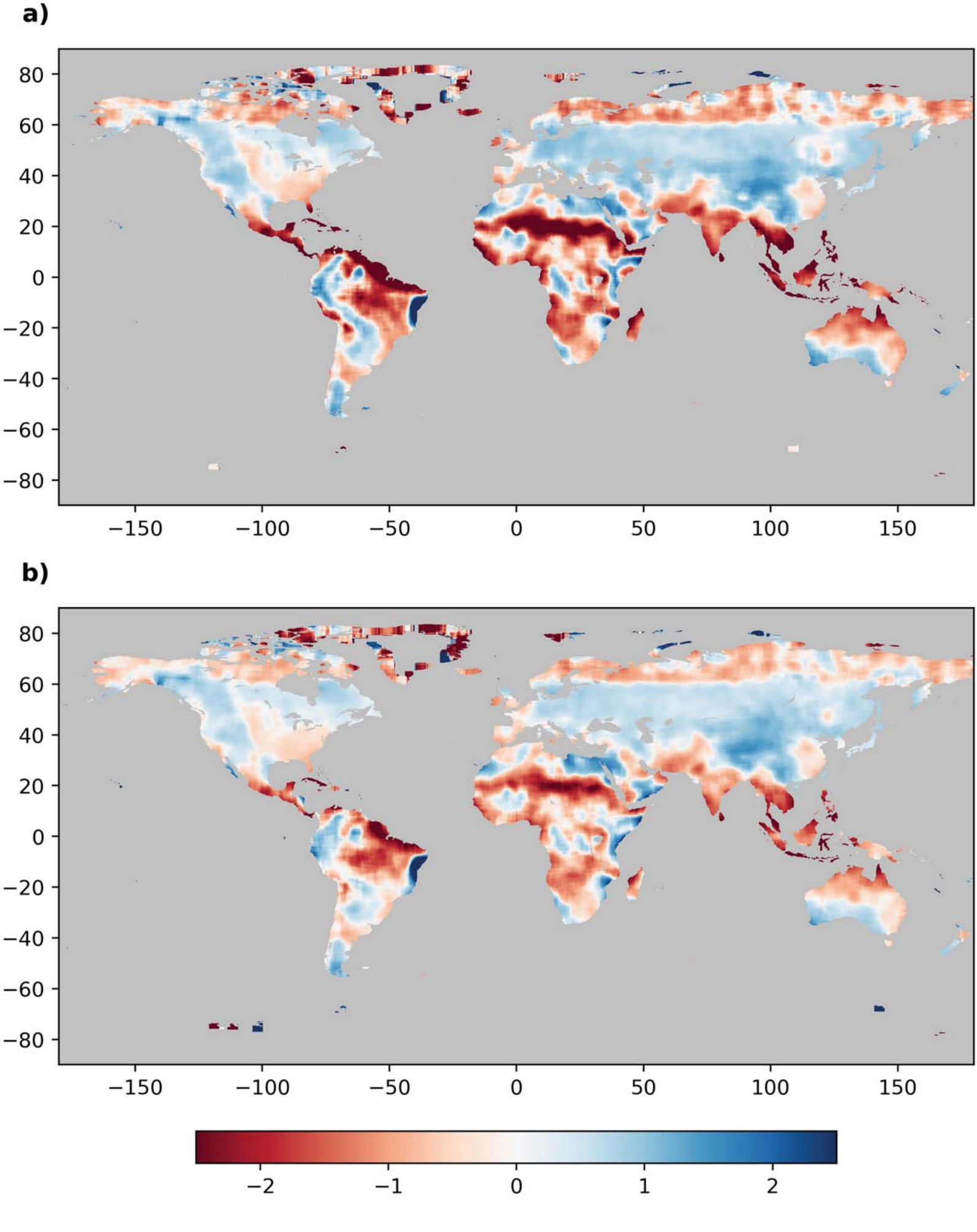
a)
b)
80
60
40
20
0
−20
−40
−60
−80
−150
−100
−50
0
50
100
150
−2
−1
0
1
2

Figure 6.

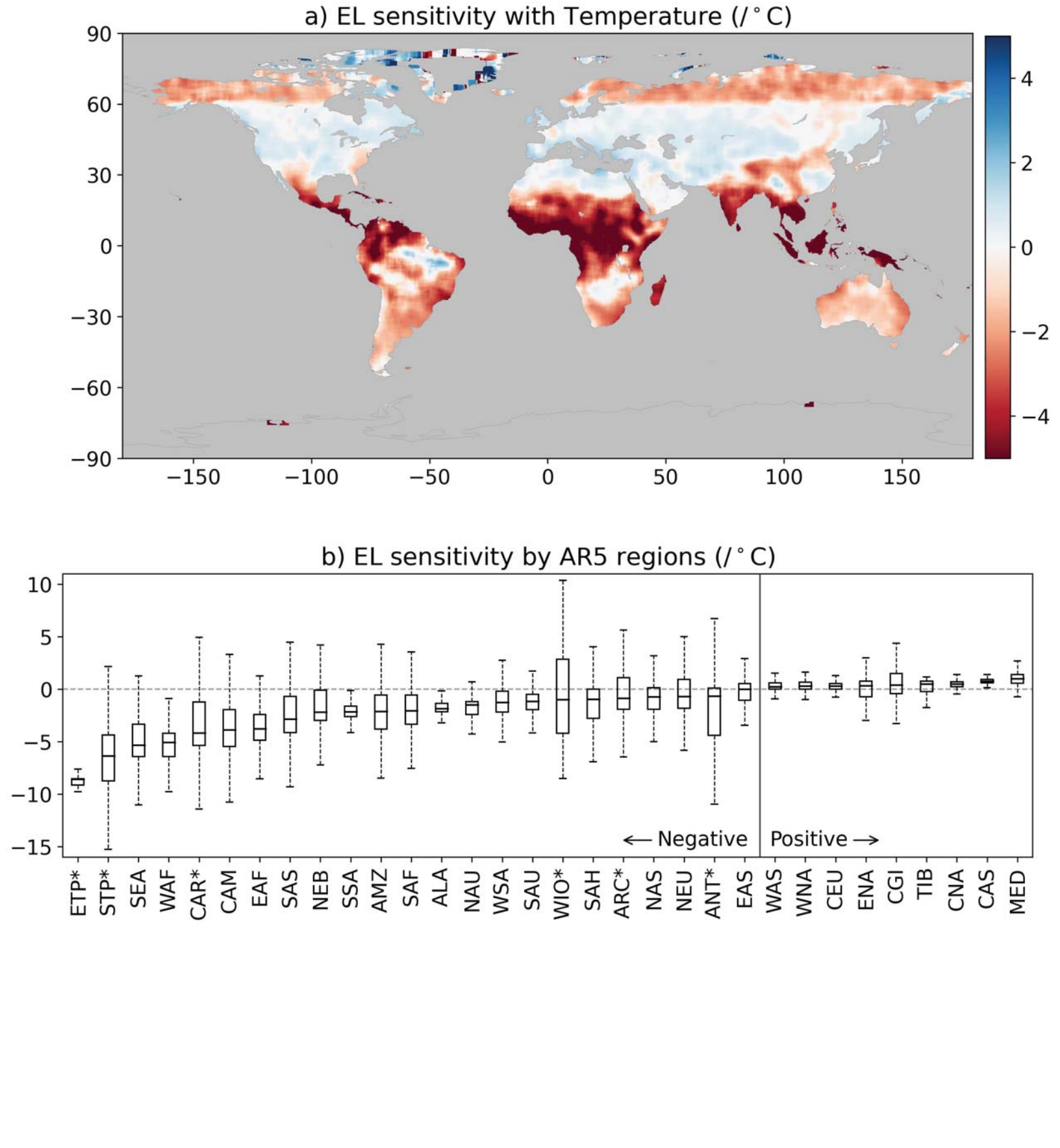
a) EL sensitivity with Temperature (/ ° C)
90
60
30
0
−30
−60
−90
−150
−100
−50
0
50
100
150
4
2
0
−2
−4
b) EL sensitivity by AR5 regions (/ ° C)
10
5
0
−5
−10
−15
← Negative
Positive →
ETP*
STP*
SEA
WAF
CAR*
CAM
EAF
SAS
NEB
SSA
AMZ
SAF
ALA
NAU
WSA
SAU
WIO*
SAH
ARC*
NAS
NEU
ANT*
EAS
WAS
WNA
CEU
ENA
CGI
TIB
CNA
CAS
MED

Figure 7.

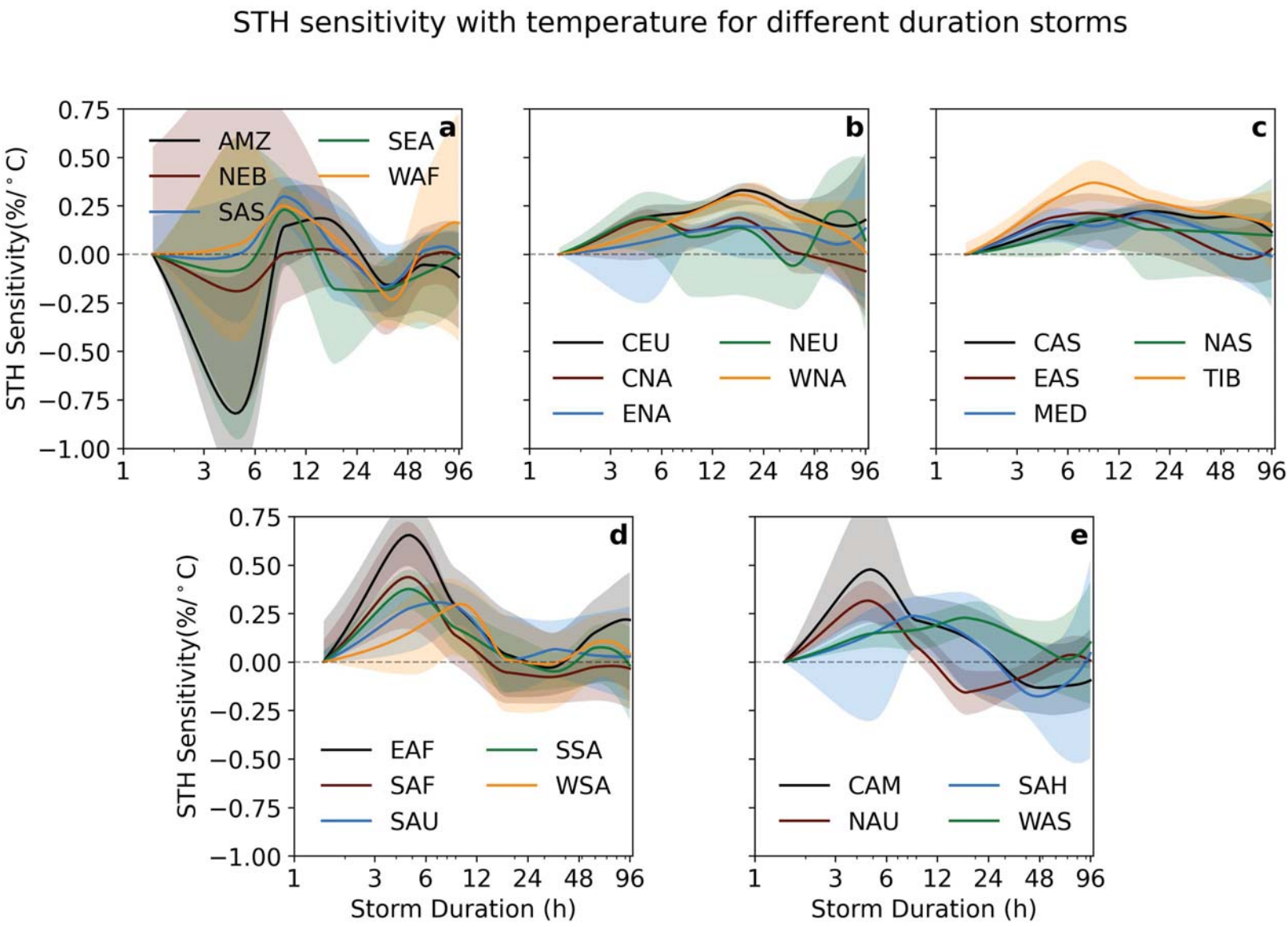
STH sensitivity with temperature for different duration storms
STH Sensitivity(%/°C)
0.75
0.50
0.25
0.00
−0.25
−0.50
−0.75
−1.00
1
3
6
12
24
48
96
a
AMZ
NEB
SAS
SEA
WAF
b
CEU
CNA
ENA
NEU
WNA
c
CAS
EAS
MED
NAS
TIB
d
EAF
SAF
SAU
SSA
WSA
e
CAM
NAU
SAH
WAS
Storm Duration (h)

Figure 8.

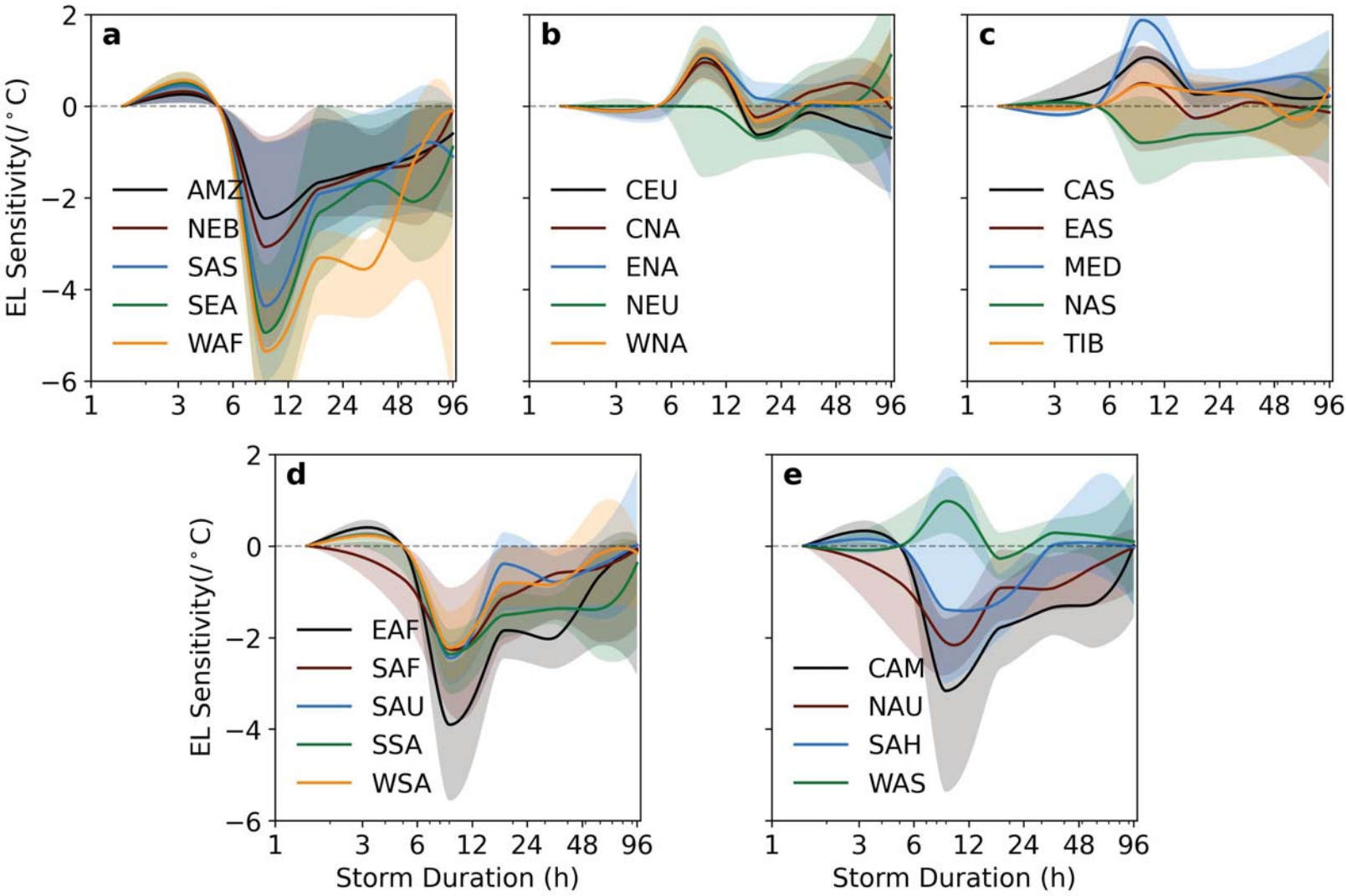
EL sensitivity with temperature for different duration storms
a
b
c
d
e
EL Sensitivity(/ ° C)
Storm Duration (h)
AMZ
NEB
SAS
SEA
WAF
CEU
CNA
ENA
NEU
WNA
CAS
EAS
MED
NAS
TIB
EAF
SAF
SAU
SSA
WSA
CAM
NAU
SAH
WAS
2
0
−2
−4
−6
1
3
6
12
24
48
96

Figure 9.

a) Spatio-temporally shrinking Front Loaded

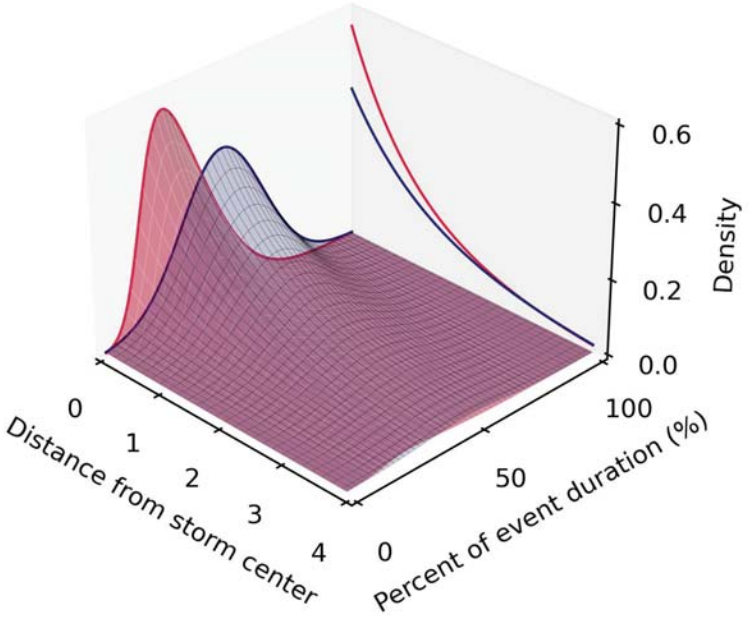

b) Spatio-temporally expanding Rear Loaded

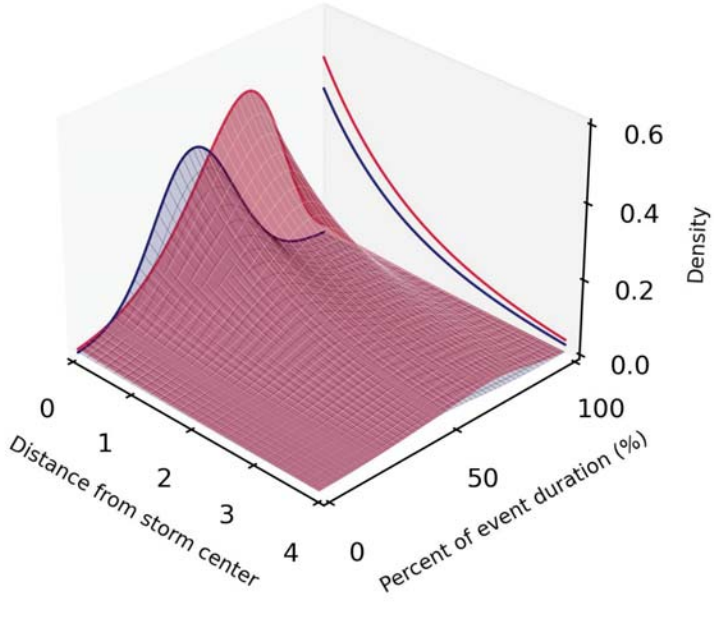

T+dT T